International Journal of Thermal Sciences 210 (2025) 109664

Contents lists available at ScienceDirect

International Journal of Thermal Sciences

journal homepage: www.elsevier.com/locate/ijts

Mixed convective laminar flow through non-circular channels heated at a constant heat flux

Qi Chen [a], Nikha Harris [b], Ken J. Craig [b], Marilize Everts [a,b,*]

[a] Department of Mechanical Engineering, University College London, London, United Kingdom
[b] Department of Mechanical and Aeronautical Engineering, University of Pretoria, Pretoria, South Africa

ARTICLE INFO

Keywords:
—Aspect ratio
Mixed convection
Non-circular channel
Developing flow
Laminar flow

ABSTRACT

Together with the need to improve the thermal efficiency, there is a continuous drive towards miniaturisation and compact heat exchangers using non-circular channels are commonly employed. In this study, mixed convective laminar flow through non-circular channels was numerically investigated using Ansys Fluent 2024R1. The hydraulic diameter of the channels was chosen as 4 mm, 8 mm, and 11.5 mm with aspect ratios (*AR*) of ½, 1, and 2, while the Reynolds number and heat flux ranges were 1000–1800 and 1–3 kW/m^2, respectively. Special attention was given to the local Nusselt number trends, velocity and temperature profiles, and circulation strength along the channels. In general, the local Nusselt numbers increased with increasing hydraulic diameter and heat flux, and decreasing Reynolds number, due to increased buoyancy effects and circulation strength. While an increase in channel height enhanced the secondary flow velocity, an increased in channel width enabled the formation of a secondary vortex pair, which significantly enhanced the thermal performance. The relationship between the circulation strength and Nusselt number was identified, and the local Nusselt numbers increased with increasing heat flux and decreasing Reynolds number. At a fixed circulation strength, improved cross-sectional mixing led to higher Nusselt numbers. The Nusselt numbers increased with decreasing aspect ratio and overall $AR = ½$ provided the best heat transfer performance for mixed convective flow through non-circular channels. When comparing the single channels results to counterflow multi-channel heat exchangers, the results correlated very well, indicating potential savings in computational costs.

1. Introduction

Advanced technological breakthroughs greatly benefit our daily lives, but simultaneously increases the need for effective thermal management to ensure safe and optimal operation. The fast development of artificial intelligence increased the use of high-performance microprocessors and the need for high-efficiency heat exchangers due to the substantial amount of heat generated by the chips and other electronic devices, especially for large computational facilities and supercomputers [1]. The combined effect of the small surface area of microprocessors and the high power consumption, results in the heat flux of a single microprocessor reaching 150–300 W/cm^2 [2], which poses a great challenge to heat dissipation systems. Furthermore, the global effort to achieve the goal of net zero, led to a surge in demand for batteries, especially in electric vehicles and energy storage facilities for solar and wind farms. Increasing the efficiency of the cooling system not only involves better control of the temperature, but also a reduction in weight, volume and pumping power. This is particularly important in electric vehicles to increase the driving range. Due to their larger heat transfer area for a fixed volume [3], thermal management using compact heat exchangers are becoming increasingly important for microprocessors [1,4], batteries [5], renewable energy systems [6], chemical process equipment [7], fission reactors [8] and nuclear fusion [9], to ensure stability, efficiency, and lifespan of the equipment. Typically, a compact heat exchanger consists of an array of micro- or mini-channels with one or several layers. Due to the larger surface area, smaller weight and easier manufacturing process, non-circular channels are commonly used.

The concept of micro- and mini-channel heat sinks was first proposed by Tuckerman and Pease in 1980 [10]. They showed that by decreasing the liquid channel to microscopic levels, the power density of microprocessors can be up to 40 times larger than those using conventional forced air heat exchangers. They also concluded that the small channel diameter and high aspect ratio would result in high surface-to-volume ratio, and hence smaller heat resistance. However, a significant

* Corresponding author. Department of Mechanical Engineering, University College London, London, United Kingdom.
E-mail address: m.everts@ucl.ac.uk (M. Everts).

https://doi.org/10.1016/j.ijthermalsci.2024.109664
Received 23 October 2024; Received in revised form 14 December 2024; Accepted 23 December 2024
Available online 27 December 2024

Nomenclature

A	Area [m^2]
A_i	Channel inner surface area [m^2]
AR	Aspect ratio [−]
C	Perimeter of inner surface at channel cross-section [m]
c_p	Specific heat at constant pressure [kJ/kg·K]
D	Hydraulic diameter [m]
D_i	Inner diameter [m]
Gr^*	Modified Grashof number [−]
Gz	Graetz number [−]
g	Gravitational acceleration [m/s^2]
H	Height [m]
h	Convective heat transfer coefficient [$W/m^2 \cdot K$]
k	Thermal conductivity [W/m·K]
L	Length [m]
$\bar{l}$	Integration path vector [−]
Nu	Nusselt number [−]
Pr	Prandtl number [−]
$\dot{q}$	Heat flux [W/m^2]
Ra^*	Modified Rayleigh number [−]
Re	Reynolds number [−]
T	Temperature [K]
T_b	Fluid bulk temperature [K]
T_f	Local mean fluid temperature [K]
T_s	Local mean inner surface temperature [K]
t	Wall thickness [m]
u, v, w	Fluid velocity at x-, y- and z-direction [m/s]
W	Width [m]
x, y	Cross-sectional positions [m]
z	Axial position [m]

Greek letters

β	Thermal expansion coefficient [1/K]
Γ	Circulation strength [m^2/s]
μ	Dynamic viscosity [kg/m·s]
ν	Kinematic viscosity [m^2/s]
ρ	Density [kg/m^3]
ρ_0	Density at the inlet [kg/m^3]
ρ_c	Maximum density along the vertical centre line [kg/m^3]
ρ_h	Density at the bottom centre [kg/m^3]

pressure drop was observed in micro-channels, which might be undesirable in some applications. It is worth keeping in mind that the pressure drop is proportional to D^5, therefore, by increasing the channel diameter to mini-channels and macro-channels, high heat transfer coefficients can be obtained with much lower pressure drops [11]. Furthermore, larger channel diameters enable larger temperature and density differences in the fluid, thus increased buoyancy effects, which increase the Nusselt number and enhance the thermal performance [12].

In recent years, many studies were devoted to enhancing the heat transfer in mini-channel heat sinks. Due to the high heat fluxes encountered, phase-change heat transfer such as flow boiling has been widely investigated [13–15]. However, regardless of the higher heat transfer coefficients, multi-phase heat transfer systems have increased complexities and additional components as the vapour needs to be condensed. For single-phase flow systems, heat transfer was effectively enhanced using nanofluids and porous media [6,16–20], as well as by adding obstacles and changing the shape of the flow path [21–25]. Furthermore, to minimise flow recirculation at the sharp edges of the channels, special attention was also given to introducing curved edges in the inlet manifolds [26]. However, considerable pressure drops were still observed using these techniques, and the complex manufacturing process and high associated manufacturing costs prevents them from being widely used. To minimise pressure drops, the flow rates are also decreased, and these heat exchangers often operate with laminar flow. This attracts research attention to enhance heat transfer using buoyancy effects, due to the simple channel geometry and lower pressure drop penalty compared to other heat transfer enhancement methods. In practice, mixed convective flow commonly exists in heat exchangers due to the fluid properties that vary with temperature. This not only enhances mixing and heat transfer inside the heat exchanger, but also affect the flow development, heat transfer coefficients and pressure drop [27–29].

For half a century, mixed convective flow through circular and non-circular channels has been comprehensively and extensively studied to increase our fundamental understanding and being able to design more efficient heat exchangers. For circular tubes, research has been done on vertical [30], inclined [31], and horizontal flow [28], investigating the Nusselt number enhancement compared to pure forced convective flow. Research carried out by Meyer and Everts [28] has shown that, compared to the Nusselt number of fully developed forced convective flow, the value for fully developed mixed convective flow in a horizontal tube could be up to 60 % higher using tubes with a diameter of 4 mm and up to 300 % when increasing the diameter to 11.5 mm.

As for non-circular channels, Taher et al. [32] numerically and experimentally studied the heat transfer characteristics of mixed convective flow in a high aspect ratio ($AR = 10$) rectangular channel with a height and width of 20 mm and 200 mm, respectively. The channel was heated from below at a constant heat flux ranging from 10 W/m^2 to 650 W/m^2 and experiments were conducted for low Reynolds numbers ranging from 25 to 100. It was found that mixed convective flow had much higher Nusselt numbers than forced convection, especially for higher Rayleigh numbers of 9.35×10^5. The fully developed Nusselt number increased to 16 compared to the corresponding theoretical forced convective Nusselt number of 3.36. The flow patterns indicated several pairs of vortices at the cross-section, which significantly enhanced the heat transfer coefficients. The number of vortex pairs increased from 6 at a Rayleigh number of 1.28×10^4 to 18 at a Rayleigh number of 1.4×10^5, with more uniform cross-sectional mixing owing to the extra vortex pairs.

Chong et al. [33] simulated the 3-D mixed convective flow in a 20 mm × 20 mm horizontal channel ($AR = 1$) heated from below. Heat transfer was enhanced due to buoyancy effects and the Nusselt number reached 20 when the flow was fully developed, which was significantly higher than for forced convective flow ($Nu = 3.61$) [34]. They also found that the average Nusselt number increased with Grashof number and Reynolds number, but the effect became minimal when increasing the Reynolds number above 1500.

Koffi et al. [35] heated a horizontal rectangular duct from one lateral vertical wall, with the other sides insulated. The duct height and width were 14 mm and 26 mm, respectively, having an aspect ratio of 1.86. The flow pattern was reported as a longitudinal roll embedded into a return flow of possibly up to 20 times the channel height of streamwise extension. The effect of buoyancy on the flow pattern was extensively investigated. According to their analysis, such a flow pattern enables fluid particles to stay longer in the heated zone so that thermal performance was enhanced. The fully developed Nusselt numbers at Rayleigh numbers of 2.83×10^5 and 1.35×10^5 were about 55 and 15, respectively. Similar duct configurations were also studied by Toriyama et al. [36]. However, they kept the height of the duct constant rather than the hydraulic diameter. In their model, the channel was heated from one lateral vertical wall and was cooled from the other lateral wall. The influence of aspect ratio was investigated, and they found that $AR = 1$

had the highest heat transfer enhancement with a fully developed Nusselt number of approximately 22.

Extensive research has been conducted on mixed convective flow through different channel geometries, focusing on the average and/or fully developed Nusselt numbers and the effect of Reynolds number, Grashof number or Rayleigh number. It has been proven that the aspect ratio of non-circular channels had a significant impact on heat transfer performance, but the development of the buoyancy-induced secondary flow and the associated effects on the local Nusselt numbers have not yet been fully investigated. In previous studies, researchers tended to choose channels with large sizes, while buoyancy effects in non-circular channels with smaller hydraulic diameters (4–10 mm) were seldom mentioned. Therefore, in this study, a numerical study using Ansys Fluent 2024 R1 was carried out to investigate the influence of aspect ratio, heat flux and Reynolds number on laminar mixed convective flow through horizontal non-circular channels with different hydraulic diameters.

The next section describes the numerical model utilised, with attention given to mesh dependency and validation. This is followed by the data reduction employed, a results section wherein effects of Reynolds number and heat flux are presented and discussed, with a final section concluding the paper.

2. Numerical model

2.1. Geometry and boundary conditions

Non-circular channels with hydraulic diameters of 4 mm, 8 mm, and 11.5 mm were numerically investigated using Ansys Fluent 2024R1. For each hydraulic diameter, three different aspect ratios (width-to-height) of ½, 1 and 2 were investigated, as summarised in Table 1. The length of the channel was sufficient to ensure fully developed flow [28]. The length-to-diameter ratio of the 11.5 mm channel was shorter than for the other hydraulic diameters, as Everts and Meyer [28] found that mixed convective flow increases with increasing tube diameter and decreases the thermal entrance length. The flow direction was defined in the z-direction and a schematic of the non-circular channel with reference frame and boundary conditions is shown in Fig. 1(a). In addition, a circular channel (Fig. 1(b)) with an inner diameter of 4 mm, a wall thickness of 1 mm, and a length of 5.9 m, was used for validation and mesh independence study.

To investigate simultaneously hydrodynamically and thermally developing flow, the inlet of the channel was set to a velocity inlet, and the velocity direction was normal to the cross-section, with zero velocity in both x and y directions. Furthermore, the inlet temperature was set to 295.92 K and the cross-section of the solid zone at the inlet and outlet were adiabatic. The material of the solid tube was set as copper. Different channel geometries were used to investigate the effect of aspect ratio, therefore the heat input to the outer wall of the channel differed, so that the corresponding heat flux on the inner wall was constant for all aspect ratios and hydraulic diameters. The inner wall of the channel was set to no-slip with thermal conditions coupled. The flow was considered to be fully developed as the length-to-diameter ratio of the channel was very large (>826 for 11.5 mm channel and >1479 for 4 mm and 8 mm channels) and sufficient for fully developed flow [27], therefore a pressure outlet was used. The equations were solved using the SIMPLE scheme, while the Least Squares Cell-Based method was applied to gradients, PRESTO! was used for pressure, and Second-Order Upwind was selected for the energy and momentum equations.

2.2. Governing equations

The flow of water through the channel was assumed to be steady, laminar, incompressible, viscous, Newtonian, without radiation and viscous heat dissipation. Although density is considered to be a function of temperature, the incompressible assumption is still made as the application is a single-phase flow where pressure effects on density are neglected. Considering these assumptions, the continuity equation was simplified to:

$$\frac{\partial u}{\partial x}+\frac{\partial v}{\partial y}+\frac{\partial w}{\partial z}=0 \tag{1}$$

where u, v, w are the velocity in the x, y, z directions, respectively. Gravity was applied to the negative direction of the y-axis, therefore the momentum conservation equations were simplified to:

$$\rho\left(u\frac{\partial u}{\partial x}+v\frac{\partial u}{\partial y}+w\frac{\partial u}{\partial z}\right)=-\frac{\partial P}{\partial x}+\frac{\partial}{\partial x}\left(2\mu\frac{\partial u}{\partial x}\right)+\frac{\partial}{\partial y}\left(\mu\left[\frac{\partial u}{\partial y}+\frac{\partial v}{\partial x}\right]\right)+\frac{\partial}{\partial z}\left(\mu\left[\frac{\partial w}{\partial x}+\frac{\partial u}{\partial z}\right]\right) \tag{2}$$

$$\rho\left(u\frac{\partial v}{\partial x}+v\frac{\partial v}{\partial y}+w\frac{\partial v}{\partial z}\right)=-\frac{\partial P}{\partial y}+\frac{\partial}{\partial x}\left(\mu\left[\frac{\partial u}{\partial y}+\frac{\partial v}{\partial x}\right]\right)+\frac{\partial}{\partial y}\left(2\mu\frac{\partial v}{\partial y}\right)+\frac{\partial}{\partial z}\left(\mu\left[\frac{\partial v}{\partial z}+\frac{\partial w}{\partial y}\right]\right)+(\rho-\rho_0)g \tag{3}$$

Table 1
Summary of the dimensions and aspect ratios of the non-circular channels investigated in this study.

No.	Hydraulic Diameter	Width	Height	Length	Thickness	Length-to-diameter Ratio	Aspect Ratio
1	4 mm	3 mm	6 mm	5.9 m	1 mm	1478.75	0.5
2	4 mm	2 mm	2 mm	5.9 m	1 mm	1478.75	1
3	4 mm	6 mm	3 mm	5.9 m	1 mm	1478.75	2
4	8 mm	6 mm	12 mm	11.8 m	1 mm	1478.75	0.5
5	8 mm	8 mm	8 mm	11.8 m	1 mm	1478.75	1
6	8 mm	12 mm	6 mm	11.8 m	1 mm	1478.75	2
7	11.5 mm	8.62 mm	17.25 mm	9.5 m	0.6 mm	826.09	0.5
8	11.5 mm	11.5 mm	11.5 mm	9.5 m	0.6 mm	826.09	1
9	11.5 mm	17.25 mm	8.62 mm	9.5 m	0.6 mm	826.09	2

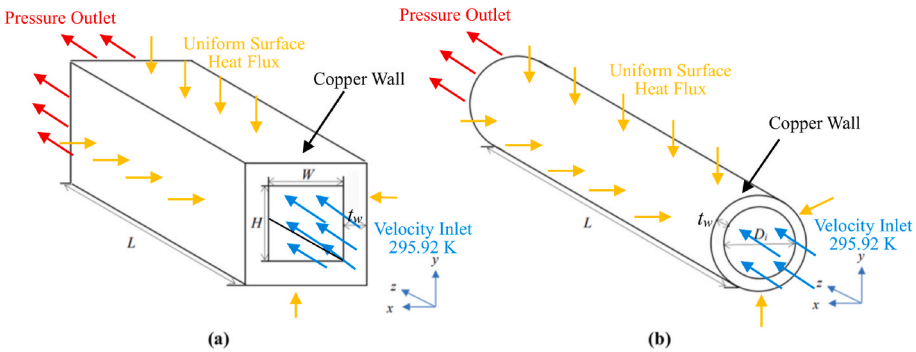

Fig. 1. Schematics of the (a) non-circular channel and (b) circular channel indicating the dimensions and boundary conditions.

Table 2
Summary of the numerical simulation matrix for the single channel investigation.

Hydraulic Diameter	Reynolds Number	Inlet Flow Velocity	Inlet Temperature	Heat Flux	Modified Grashof Number	Aspect Ratio
4 mm	1800	0.4231 m/s	295.92 K	1 kW/m^2	1.26×10^3	½, 1, 2
4 mm	1000	0.2351 m/s	295.92 K	3 kW/m^2	6.51×10^3	½, 1, 2
8 mm	1800	0.2116 m/s	295.92 K	1 kW/m^2	2.31×10^4	½, 1, 2
8 mm	1800	0.2116 m/s	295.92 K	3 kW/m^2	1.11×10^5	½, 1, 2
8 mm	1400	0.1645 m/s	295.92 K	3 kW/m^2	1.33×10^5	½, 1, 2
8 mm	1000	0.1175 m/s	295.92 K	3 kW/m^2	1.78×10^5	½, 1, 2
8 mm	1000	0.1175 m/s	295.92 K	2 kW/m^2	8.40×10^4	½, 1, 2
8 mm	1000	0.1175 m/s	295.92 K	1 kW/m^2	2.82×10^4	½, 1, 2
11.5 mm	1800	0.1469 m/s	295.92 K	1 kW/m^2	9.37×10^4	½, 1, 2
11.5 mm	1000	0.0816 m/s	295.92 K	3 kW/m^2	6.24×10^5	½, 1, 2

Table 3
Summary of the numerical simulation matric for the multi-channel investigation using channels with a hydraulic diameter of 11.5 mm.

Heat input location	Reynolds Number	Heat Input	Heat flux	Modified Grashof Number	Aspect Ratio
Uniform	1800	1000 W	1.87 kW/m^2	2.64×10^5	½
Uniform	1800	1000 W	2.08 kW/m^2	2.99×10^5	1
Uniform	1800	1000 W	1.87 kW/m^2	2.64×10^5	2
Left and right surfaces	1800	1000 W	2.87 kW/m^2	2.64×10^5	½
Top and bottom surfaces	1800	1000 W	4.16 kW/m^2	2.98×10^5	1
Left and right surfaces	1800	1000 W	4.16 kW/m^2	2.98×10^5	1
Top and bottom surfaces	1800	1000 W	2.87 kW/m^2	2.64×10^5	2

$$\rho\left(u\frac{\partial w}{\partial x}+v\frac{\partial w}{\partial y}+w\frac{\partial w}{\partial z}\right)=-\frac{\partial P}{\partial z}+\frac{\partial}{\partial x}\left(\mu\left[\frac{\partial w}{\partial x}+\frac{\partial u}{\partial z}\right]\right)+\frac{\partial}{\partial y}\left(\mu\left[\frac{\partial v}{\partial z}+\frac{\partial w}{\partial y}\right]\right)+\frac{\partial}{\partial z}\left(2\mu\frac{\partial w}{\partial z}\right) \quad (4)$$

where P is pressure, ρ is fluid density, ρ_0 is fluid density at the inlet, g is gravitational acceleration, and μ is dynamic viscosity of fluid. The energy conservation equation, with no viscous work and radiation, is given by:

$$\rho c_p\left(u\frac{\partial T}{\partial x}+v\frac{\partial T}{\partial y}+w\frac{\partial T}{\partial z}\right)=\frac{\partial}{\partial x}\left(k\frac{\partial T}{\partial x}\right)+\frac{\partial}{\partial y}\left(k\frac{\partial T}{\partial y}\right)+\frac{\partial}{\partial z}\left(k\frac{\partial T}{\partial z}\right) \quad (5)$$

where c_p is specific heat of the fluid, T is the fluid temperature, and k is the thermal conductivity of the fluid. Since the density and thermal properties of water changes with temperature, and these properties significantly influence the buoyancy effects, the thermophysical correlations proposed by Popiel and Wojtkowiak [37] were used.

2.3. Numerical simulation matrix

As summarised in Table 2, simulations were conducted for channels with different hydraulic diameters and aspect ratios at Reynolds numbers of 1000, 1400 and 1800, and wall heat fluxes of 1, 2 and 3 kW/m^2. As the focus of this study was on mixed convective laminar flow through non-circular channels, the heat fluxes were chosen such to prevent the temperatures from approaching saturation temperature and thus ensuring single-phase flow. Furthermore, as it is known from previous studies on circular tubes [38] that the transition to turbulence occurs earlier when decreasing the tube diameter or increasing the heat flux, the Reynolds number range was kept below 2000 to ensure laminar flow along the entire tube length. To ensure that the heat fluxes were sufficient to investigate mixed convective flow, the flow regime map of Everts and Meyer [38], which was developed for circular tubes heated at

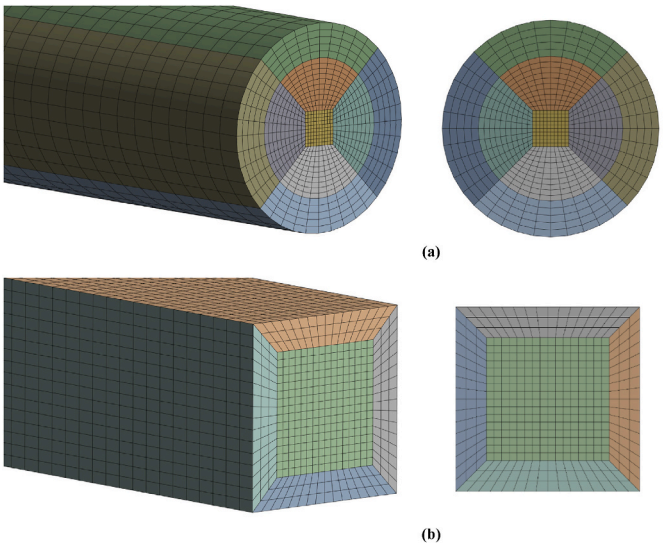

Fig. 2. Sample axial and cross-sectional mesh structures for the (a) circular and (b) non-circular channels.

a constant heat flux, was used as a guideline. Based on the flow regime maps, forced convective flow was expected for the 4 mm channel at a Reynolds number of 1800 and heat flux of 1 kW/m^2, some mixed convective effects at a Reynolds number of 1000 and heat flux of 3 kW/m^2, and mixed convective flow for the larger channels at both 1 kW/m^2 and 3 kW/m^2 heat fluxes.

Furthermore, to investigate the scalability of the single-channel results to multi-channel counterflow heat exchangers, four multi-channel systems were investigated, and the simulation parameters are summarised in Table 3. For comparison purposes between the single and multi-channel results, the heat input to these channels were kept constant, which resulted in different heat fluxes due to the different heat transfer surface areas.

2.4. Mesh independence and validation

Highly structured meshes were generated for the circular and non-circular channels. The circular tube was used for the mesh independence study and validation. As indicated in Fig. 2(a), the cross-sectional fluid zone was divided into five parts, consisting of a square core and four surrounding zones, to ensure uniformity and high-quality hexahedral cells. Since the flow was laminar, inflation was unnecessary for resolving the boundary layers. In the entrance region, the temperature and velocity profiles were both developing, therefore the mesh density in this area was greater and a bias number of 15 was used along the length of the tube.

Different mesh sizes ranging from 41 400 to 2 587 500 were evaluated at a Reynolds number of 2000 and inlet temperature of 295.92 K. The local Nusselt number along the channel and vertical temperature distribution of the fluid at $z = 0.14$ m are compared for the circular channel in Fig. 3. Mesh numbers 1 to 4 correspond to mesh sizes of 41 400, 145 000, 576 000, and 2 587 500 elements. From this figure it follows that minor differences were observed for Mesh 1 and 2, while the difference in results obtained using Mesh 3 and 4 became negligible. As the results of the local Nusselt number and temperature profile only changed by approximately 1.25 % when increasing the mesh size from 576 000 to 2 587 500, Mesh 3 (576 000 elements) was chosen as the optimal mesh size and was used in the validation. In the radial direction, the element size of the fluid and solid zones were 0.0002 m and 0.0003 m, respectively, while the largest element size in the tangential direction was 0.0006 m. In the flow direction, the element size gradually increased from 0.0008 m at the inlet to 0.012 m at the outlet. Based on the findings of the mesh independence study on the circular channel, similar structured meshes were generated for the non-circular channels, as indicated in Fig. 2(b). However, the number of elements increased to 806 400 due to the larger cross-sectional areas of the non-circular channels.

The validation was conducted at a Reynolds numbers of 1000 and heat fluxes of 1 and 3 kW/m^2. The results were compared with the experimental data from Meyer and Everts [27] and the theoretical forced Nusselt number of 4.36 for fully developed forced convective flow through a circular tube [39] in Fig. 4. The error bars indicate the experimental uncertainties of the local Nusselt numbers, which had an average uncertainty of ±10 % and ±4 % for the forced (Fig. 4(a)) and mixed (Fig. 4(b)) convective data, respectively. Fig. 4(a) indicated that the forced convective simulation results and experimental data corresponded very well, with an average deviation of 3.58 %. The local Nusselt number decreased from the inlet of the tube and became approximately constant as the flow approached fully developed flow. The average fully developed Nusselt number was approximately 4.66, confirming forced convective flow, as it was within 10 % of the theoretical forced convective Nusselt number. It follows from Fig. 4(b), that the simulation data corresponded well with the mixed convective experimental data of Meyer and Everts [27], with an average deviation

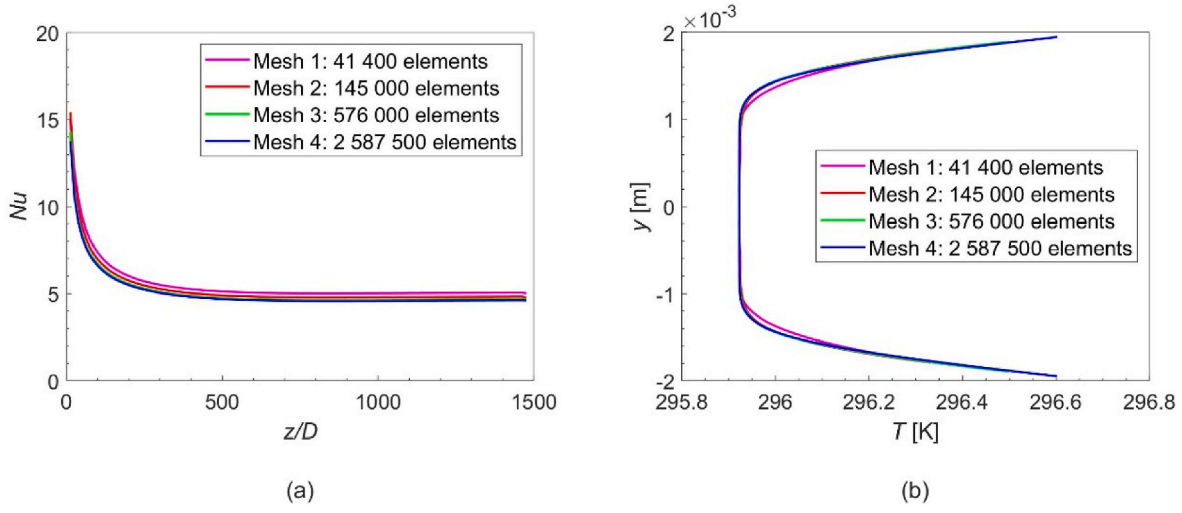

Fig. 3. Mesh independence study at $Re = 2000$ by comparing (a) the local Nusselt number and (b) the fluid temperature profile at $x = 0$ m and $z = 0.14$ m in the 4 mm circular channel.

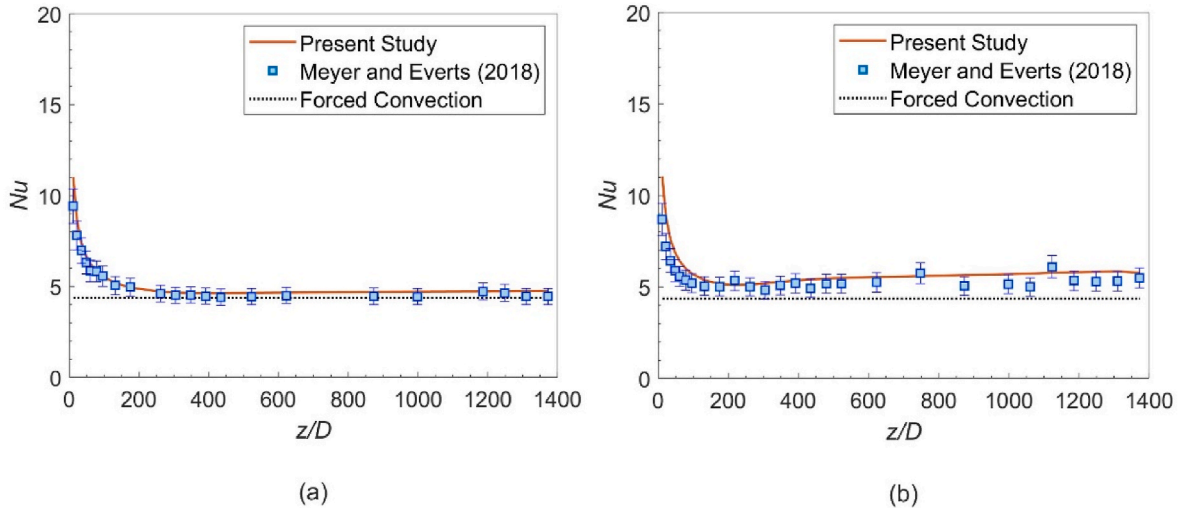

Fig. 4. Comparison of the local Nusselt number along the length of the 4 mm circular channel with the experimental data of Meyer and Everts [8] and theoretical fully developed forced convective Nusselt number [19] at (a) $Re = 1\ 000$, $\dot{q} = 1$ kW/m^2 (forced convection) and (b) $Re = 1\ 000$, $\dot{q} = 3$ kW/m^2 (mixed convection).

of 8.6 %. Unlike the forced convective trend in Fig. 4(a), the local Nusselt numbers in Fig. 4(b) continued to increase along the tube length to a Nusselt number of 5.48 near the outlet. As this was 26 % greater than the theoretical forced convective Nusselt number, it confirmed the predictions of the flow regime map of Everts and Meyer [38] that mixed convection conditions existed.

3. Data reduction

The mean cross-sectional fluid temperature at a specific axial location along the channel, was calculated using the mass-averaged method [40]:

$$T_f = \frac{\iint_A T\rho w dA}{\iint_A \rho w dA} \tag{6}$$

where w is the fluid velocity magnitude in the z-direction, and A is the cross-section area ($A = \pi D_i^2/4$). The bulk fluid temperature was determined by averaging the inlet, T_i, and outlet, T_o, temperature:

$$T_b = \frac{T_i + T_o}{2} \tag{7}$$

The mean inner wall temperature of the cross-section at a specific axial position of the channel was calculated by taking the average value of the temperature around the cross-section:

$$T_s = \frac{1}{C}\oint_C T dC \tag{8}$$

where C is the perimeter of channel inner cross-section ($C = \pi D_i$). The channel hydraulic diameter was defined as:

$$D = \frac{4WH}{2(W+H)} \tag{9}$$

where W and H are the width and height of the inner cross-section. The convective heat transfer coefficient h was obtained by:

$$h = \frac{\dot{q}}{T_s - T_f} \tag{10}$$

where $\dot{q}$ is the heat flux on the inner wall. The Nusselt number was then obtained by:

$$Nu = \frac{hD}{k} \tag{11}$$

where D is the channel hydraulic diameter. The Reynolds number was defined as:

$$Re = \frac{\rho w D}{\mu} \tag{12}$$

As a constant heat flux was applied to the channels, the modified Grashof number and modified Rayleigh number were used this study:

$$Gr^* = \frac{g\beta\dot{q}D_h^4}{\nu^2 k} \tag{13}$$

$$Ra^* = Gr^* Pr \tag{14}$$

where β is thermal expansion coefficient, ν is the kinematic viscosity ($\nu = \mu/\rho$), and Pr is the Prandtl number ($c_p\mu/k$). The fluid properties were evaluated at bulk fluid temperature, T_b, using the thermophysical correlations of water proposed by Popiel and Wojtkowiak [37]. In addition, the Graetz number was determined as:

$$Gz = RePr\frac{D}{z} \tag{15}$$

To quantitively investigate mixed convective flow, the circulation strength was defined as the integral of the secondary in-plane flow velocity along a closed loop which enclosed the vortex core:

$$\Gamma = \oint_l \overline{\boldsymbol{V}} \cdot d\bar{l} \tag{16}$$

where $\bar{l}$ is the path vector and $\overline{\boldsymbol{V}}$ the component of the velocity vector in the x-y plane. Due to the symmetrical behaviour of the vortices, the circulation strength was only calculated for one side.

4. Results and discussion

4.1. Local Nusselt number

The local Nusselt numbers along the channels with different aspect ratios are compared in Fig. 5 for the 4 mm, 8 mm, and 11.5 mm channels at the highest modified Grashof number ($Re = 1000$, $\dot{q} = 3$ kW/m^2) and the lowest modified Grashof number ($Re = 1800$, $\dot{q} = 1$ kW/m^2). For channels with a hydraulic diameter of 4 mm at a low modified Grashof number of 1.26×10^3, the Nusselt number in the entrance region at $z/D = 11.75$ was 14.36, which was almost the same for all aspect ratios. The local Nusselt numbers decreased along the length as the boundary layer

developed and became constant for $z/D > 600$ as the flow became fully developed. The fully developed Nusselt numbers of $AR = ½$ and $AR = 2$ were 4.31 and 4.36 respectively, while the Nusselt number of $AR = 1$ was 4.02 and 4.64 for the circular tube. The theoretical Nusselt numbers of fully developed forced convective flow in square ($AR = 1$) and rectangular channels ($AR = ½$ or 2) are 3.61 and 4.12, respectively, and 4.36 for a circular tube [34]. This indicates that the buoyancy effects were minor with 4.61 %–11.36 % enhancement. The flow was considered to be forced convective with the heat transfer surface area being the controlling factor. As the surface area of $AR = ½$ and $AR = 2$ were the same, their fully developed Nusselt numbers were very close. The inner surface area of the rectangular channel was 1.125 times larger than for the square channel, which corresponded well with the Nusselt number enhancement of 1.1 times. Although the heat transfer surface area was smaller for the circular tube, the smooth and curved geometry was more effective in enhancing buoyancy effects and heat transfer. This is due to the stagnant fluid areas near the corners of the non-circular channels, as will be discussed in Fig. 8. Therefore, although non-circular channels are preferred in compact heat exchangers to minimise space and material requirements, it is worth keeping in mind that, depending on the significance of buoyancy effects, the thermal performance could be slightly less than when using circular tubes.

For a higher modified Grashof number of 6.51×10^3, increased buoyancy effects were observed which led to changes in the local Nusselt number trends. The Nusselt number in the entrance region was lower as it developed faster [28], and decreased from approximately 11 at $z/D = 11.75$ to approximately 4.6 at $z/D = 200$. Thereafter, it increased due to the development of secondary flow which enhanced heat transfer, and finally reached Nusselt numbers of 5.84, 5.47, 5.29 and 5.24, respectively for the circular tube and non-circular channels with $AR = ½$, $AR = 1$ and $AR = 2$, respectively, at $z/D = 1373$. As the buoyancy effects increased and became dominant, the increased surface area of the non-circular channels played a less important role, although there were still minor differences between the different aspect ratios. As a result of the small hydraulic diameter and large surface-to-volume ratio, the cross-sectional temperature difference within the fluid was relatively small, but sufficient to lead to Nusselt number enhancements of approximately 30 % compared to that of forced convection.

Fig. 5(b)and (c) indicates that the local Nusselt numbers significantly increased as the hydraulic diameter increased to 8 mm and 11.5 mm. This is as expected as the modified Grashof number in Eq. (14) is proportional to D^4, indicating that a small increase in channel diameter has potential for a significant increase in buoyancy effects. The increasing local Nusselt numbers along the channel length were because of the increasing wall-fluid temperature difference along the channel, which led to higher density gradients within fluid and thereby stronger secondary flow, as will be discussed in Section 4.2.1. At lower modified Grashof numbers, the local Nusselt number trends were the same for all three hydraulic diameters with the maximum fully developed Nusselt numbers obtained for $AR = ½$ and followed by $AR = 1$ and $AR = 2$. The difference in Nusselt number among different channel aspect ratios increased with increasing hydraulic diameter, especially at the highest Grashof number, due to higher density gradient and greater buoyancy effects.

Furthermore, at higher modified Grashof numbers in the 8 mm and 11.5 mm channels, local peaks existed in the local Nusselt number trends, which led to increased Nusselt numbers. This was due to the formation of a secondary vortex pair which is investigated in detail in Section 4.2. As the buoyancy effects were increased by increasing the channel diameter from 8 mm to 11.5 mm, these peaks occurred earlier along the tube length and increased in magnitude as well. Furthermore, the peaks occurred earlier with increasing aspect ratio. For $AR = 2$, significant fluctuations were observed for $100 < z/D < 450$, indicating possible transient behaviour. An interesting conclusion from Fig. 5(c) is that both in the absence (low modified Grashof numbers) and presence (high modified Grashof numbers) of the secondary vortex pair, best thermal performance for mixed convective flow was obtained for $AR = ½$.

When plotting the results of the different hydraulic diameters and aspect ratios on the flow regime map of Everts and Meyer [38] in Fig. 6, it is evident that mixed convective flow increases with increasing hydraulic diameter. Furthermore, when comparing the magnitude of the Nusselt numbers to those predicted using the flow regime map, the flow regime map underpredicted the Nusselt numbers in the non-circular channels by 6 %, and 13 % for hydraulic diameters of 8 mm and 11.5 mm, while the 4 mm results were comparable. Furthermore, no significant differences were observed for the different aspect ratios when using this flow regime map. This indicates that although the circular tube flow regime maps could predict the significance of buoyancy effects, it could not accurately predict the effect of buoyancy effects on the heat transfer coefficients. The mixed convective behaviour is more complex in non-circular channels due to the formation of secondary

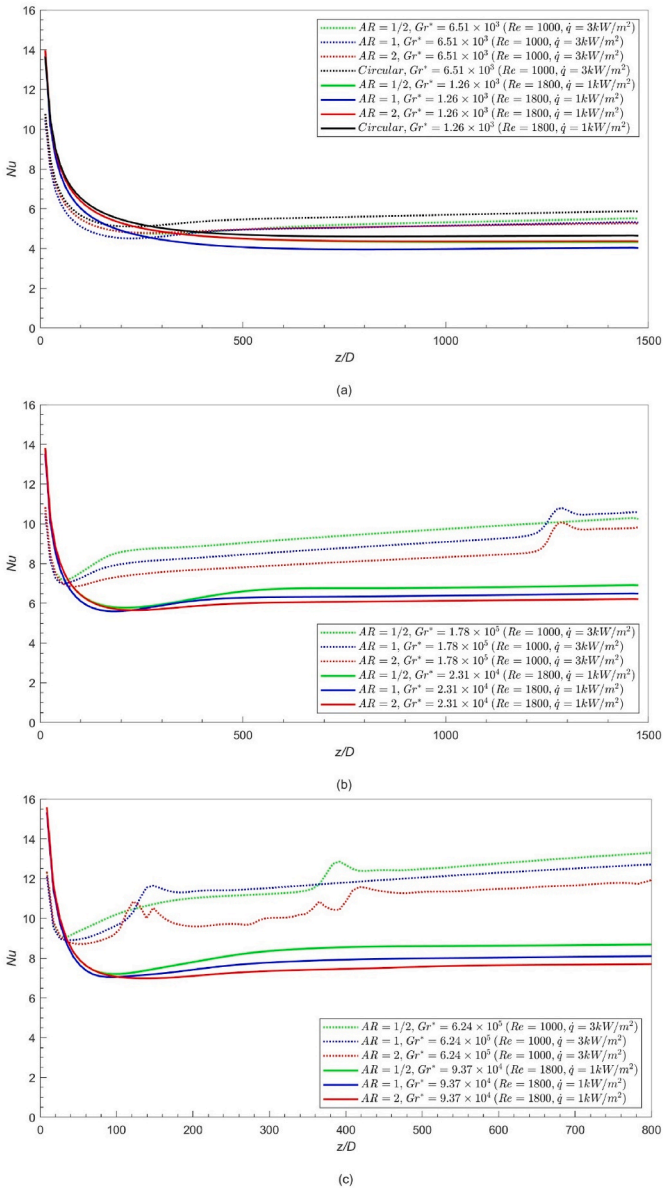

Fig. 5. Comparison of the local Nusselt number as a function of axial position for different aspect ratios and modified Grashof numbers in (a) 4 mm, (b) 8 mm, and (c) 11.5 mm channels. The dotted lines represent a Reynolds number of 1000 and a heat flux of 3 kW/m^2, while the solid lines represent a Reynolds number of 1800 and a heat flux of 1 kW/m^2.

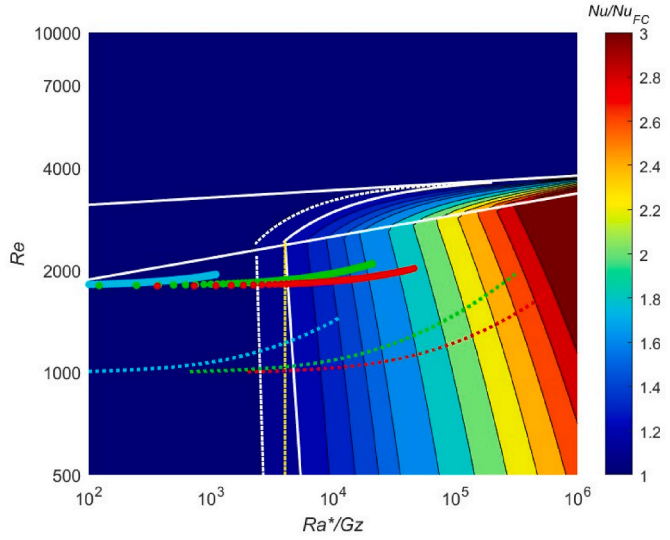

Fig. 6. Prediction of mixed convective effects in the 4 mm (cyan), 8 mm (green) and 11.5 mm (red) channels using the flow regime map of Everts and Meyer [38]. The dotted lines represent a Reynolds number of 1000 and a heat flux of 3 kW/m^2, while the solid lines represent a Reynolds number of 1800 and a heat flux of 1 kW/m^2.

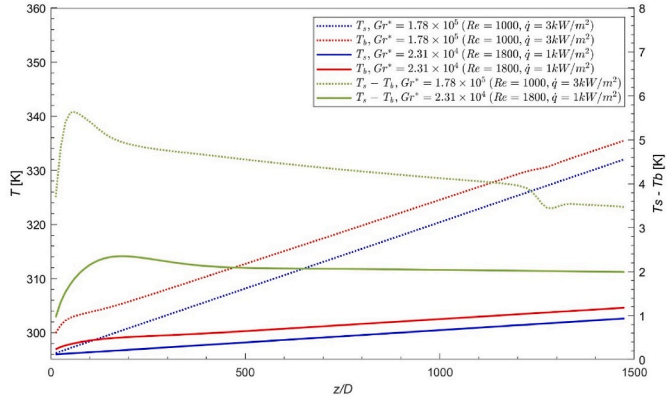

Fig. 7. Local wall and fluid temperatures and the wall-fluid temperature difference along the 8 mm channel with $AR = 1$ at different modified Grashof numbers.

vortex pairs, and it is therefore recommended that similar flow regime maps be developed for non-circular channels.

4.2. Development of secondary flow

4.2.1. Temperature profile

To investigate the development of the local temperature profiles along the channel length, Fig. 7 compares the average fluid and wall temperatures, as well as the wall-fluid temperature difference along the 8 mm channel for $AR = 1$. At low modified Grashof numbers, the temperature of the wall and fluid only increased by 8.22 K and 6.22 K, respectively, due to the relatively low heat flux and high mass flow rate. When the modified Grashof number increased, the wall and fluid temperature at $z/D = 1373$ reached 333.07 K and 329.54 K, indicating an increase of more than 33 K. The larger wall-fluid temperature difference also indicates greater potential for secondary flow.

As the flow is simultaneously hydrodynamically and thermally developing, the thermal boundary layer thickness near the channel inlet was not sufficient for buoyancy effects to become significant. The wall-fluid temperature difference, as well as the magnitude of the fluid temperature, increased from the inlet to a maximum at approximately $z/D = 60$ for the high modified Grashof number case and at $z/D = 80$ for the low modified Grashof number case. These peaks in the wall-fluid temperature differences also corresponded to the troughs in the local Nusselt numbers in Fig. 5(b). Thereafter, the secondary flow became significant and increased mixing within the channel, which enhanced heat transfer and decreased the wall-fluid temperature difference in Fig. 7 which led to increased local Nusselt numbers in Fig. 5(b). For $z/D > 150$ at $Gr^* = 1.78 \times 10^5$ and $z/D > 200$ at $Gr^* = 2.31 \times 10^4$, the temperature difference and the secondary flow velocity reached a balance, and the wall-fluid temperature difference slowly decreased because of the improved cross-sectional mixing caused by increased secondary flow velocity and increased thermal conductivity of water with increasing fluid temperature. Near the outlet, a minor decrease in the wall temperatures for the higher modified Grashof number (dotted red line) led to a sudden decrease in the wall-fluid temperature difference (dotted green line) and an increase in the local Nusselt numbers in Fig. 5(b).

To gain a better understanding of the sudden decrease in the wall-fluid temperature differences in Fig. 7, Fig. 8 compares the cross-sectional temperature profiles and streamlines at different axial positions in the 8 mm channels at a modified Grashof number of 1.78×10^5. Near the inlet of the channel ($z/D = 11.75$), where the secondary flow was developing, the low temperature (blue) region in the fluid was large. Due to the channel being heated at a constant heat flux, the fluid near the channel wall had a higher temperature, and the heated fluid rose because of its lower density, while the colder and higher density fluid at the core sank. This led to the formation of a pair of symmetrical vortices on the left and right sides of the channels as the flow continued downstream. With the development of the vortical flow and its associated mixing effect, the low temperature region gradually decreased and moved towards the bottom of the channel. This was because the warmer and lower density fluid raised towards the top of the channel, which gradually increased the high temperature region along the channel length.

As indicated by the streamlines, the cold fluid from below could no longer rise to the top of the channel, leading to thermal stratification. When comparing the upper and lower parts of the channels, it is evident that the high temperature region participated less in the secondary flow phenomena, which led to lower heat transfer coefficients in that region. This also explains why $AR = ½$ generally had the highest Nusselt numbers in Fig. 5. The smaller surface area at the top of the channel ensured that a larger proportion of fluid could effectively participate in the vortical flow, resulting in better cross-sectional mixing. By contrast, $AR = 2$ which has the largest surface area at the top, had the lowest Nusselt number. The streamlines also indicate that the cores of the vortices moved towards the bottom of the channel as the flow progressed through the channel. It is worth noting that for $AR = ½$, the downward movement of the vortices was more significant than for the other aspect ratios, indicating stronger secondary flow (as will be shown in Fig. 11) and explains why the local Nusselt numbers in Fig. 5(b) were the highest for $z/D < 1248$.

For all three aspect ratios, the cross-sectional temperature gradient changed significantly between $z/D = 61$ to $z/D = 261.75$. This was more evident in the upper part of the channel than the lower part. Thereafter, there were negligible differences in the cross-sectional temperature gradient until approximately $z/D = 1\,248$, when a secondary vortex pair formed at the bottom centre of $AR = 1$ and $AR = 2$. Further downstream, the local temperature gradient decreased, and the central low temperature region was divided into two separate zones. The upward flow of the warmer fluid in the secondary vortices was disrupted and cooled down by the downward flow of the primary vortices, causing it to move downwards instead of moving further upwards.

The additional mixing caused by the secondary vortex pair enhanced heat transfer and led to a sudden increase in the local Nusselt numbers near the outlet in Fig. 5(b). The lower wall-fluid temperature difference

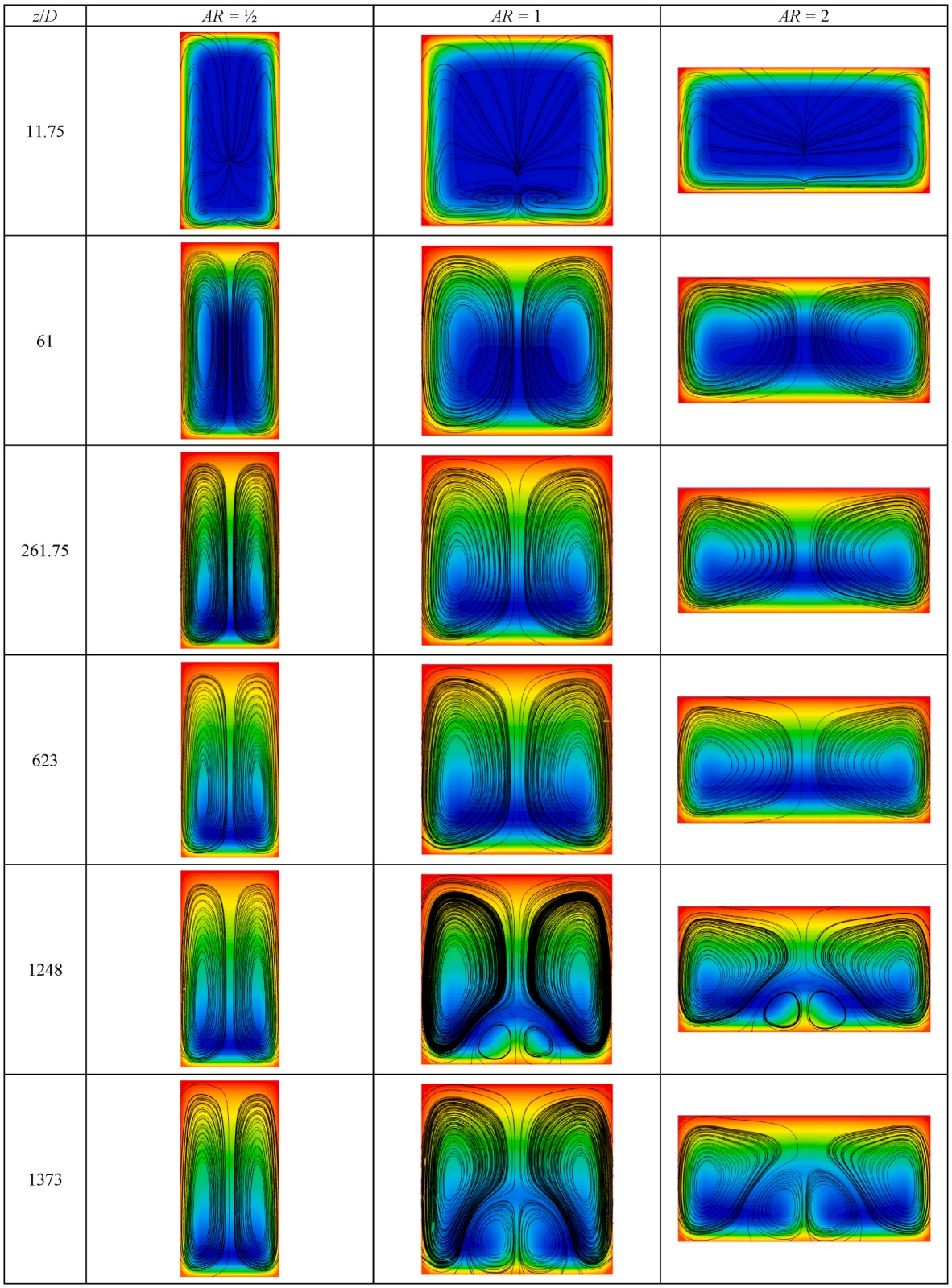

Fig. 8. Cross-sectional temperature profile and streamlines at different axial positions for $AR = ½$, 1 and 2 in the 8 mm channels at $Gr^* = 1.78 \times 10^5$ ($Re = 1000$, $\dot{q} = 3$ kW/m^2).

due to the enhanced mixing also led to a decrease in density gradient and thus buoyancy effects, which explains the slight decrease in the local Nusselt numbers after the peak, as shown in Fig. 5(b) at $z/D = 1373$. Moreover, the secondary vortex pair assisted in transferring some of the warmer fluid near the bottom centre of the channel upwards, which resulted in a higher temperature in the centre of the channel, especially in $AR = ½$, where the secondary flow velocity was the highest. The trend of the cross-sectional temperature contours in $AR = ½$ remained unchanged for $z/D > 261.75$. As the primary vortices were strong and very close to each other, it was difficult for the warmer fluid to accumulate at

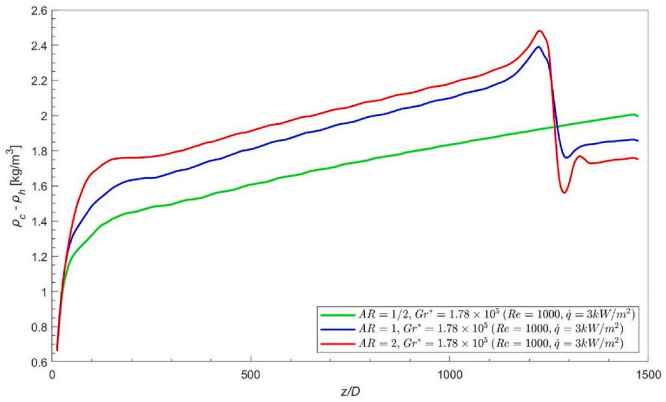

Fig. 9. Maximum density difference along the vertical centre line ($x = 0$ m) at different axial positions along the 8 mm channels at $Gr^* = 1.78 \times 10^5$ ($Re = 1000$, $\dot{q} = 3$ kW/m^2).

the centre bottom area, as it was rapidly removed and replaced by colder fluid from the centre. The strong primary vortices and their large coverage also prevented a secondary vortex pair from being generated.

Due to the non-linear relationship of density with temperature, the temperature difference was inadequate to reflect the changes in the density difference, which is key to buoyancy effects. Therefore, to gain a deeper understanding of the buoyancy effects and the development of the secondary vortex pair, the density difference between the flow centre (colder blue region in Fig. 8) and the bottom centre of the 8 mm channels at a modified Grashof number of 1.78×10^5 ($Re = 1000$, $\dot{q} = 3$ kW/m^2) was compared in Fig. 9. The density difference was calculated as the difference between the minimum density (ρ_c) at the bottom of the channel and the maximum density (ρ_h) near the centre along the vertical centre line ($x = 0$ m) of the channel.

It can be seen in Fig. 9 that the local density difference increased rapidly near the inlet of the channel, where the temperature profile and secondary flow were still developing, and later increased linearly from $z/D = 250$ when it reached a balance with the secondary flow velocity. It is worth noting that despite the decreasing temperature difference in Fig. 7, the local density difference increased along the channel as a result of the non-linear change of the density of water with temperature, as well as the continuous increase in temperature along the length due to the constant heat flux being applied.

Between $z/D = 50$ and $z/D = 1250$, the local density difference in $AR = 2$ was the highest because of the poor mixing effect at the centre bottom of the channel. Due to relatively large width of the channel, the warmer fluid at the bottom had to travel a longer horizontal distance to the vertical walls before moving upwards. This resulted in the development of a local higher temperature region at the bottom of the channel, particularly near the centre (as indicated in Fig. 8), which was the farthest from the vertical walls and was not reached by primary vortices. Consequently, the local density difference increased and once the local density difference in $AR = 1$ and $AR = 2$ were large enough (at $z/D = 1200$), the accumulated warmer fluid near the bottom centre began to rise and a secondary vortex pair developed. The increased mixing caused by the additional vortices, led to a sudden decrease in the density difference, as evident in Fig. 9. However, the low local density difference led to lower secondary flow velocity and poorer mixing effect, which increased the local density gradient again. Due to the continuous increase in temperature along the channel (due to the constant heat flux boundary condition), the local density difference reached a balance with the secondary flow velocity at $z/D = 1350$ and gradually increased with temperature.

The magnitude of the density difference for $AR = 2$ was smaller than $AR = 1$ for $z/D > 1250$. This was because the secondary vortex pair reached approximately 55 % of the channel height in $AR = 2$, which significantly increased the fluid temperature and reduced its density at the centre of the channel. For $AR = 1$, the value was only 40 %, and the temperature at the centre of the channel was still very low.

Due to the small channel width of $AR = ½$, the warmer fluid at the bottom did not have to travel a long horizontal distance before rising, and could quickly interact with the primary vortices, which prevented the warmer fluid from accumulating and reduced the local density difference. Hence, when $z/D > 200$, the density difference continued increasing linearly as there were no secondary vortices, and it exceeded the values of $AR = 1$ and $AR = 2$ when $z/D > 1250$ but was less than the maximum values of $AR = 1$ and $AR = 2$. This indicates that the width of the channel was the key factor for the formation of secondary vortices, as it could significantly influence the density difference at the bottom centre. When the hydraulic diameter of the channel is increased, the local density difference increases as well, and secondary vortices would also appear in $AR = ½$, as indicated in Fig. 5(c).

4.2.2. Velocity profile

Velocity vector graphs of the secondary flow at different axial positions along the 8 mm channels are compared in Figs. 10 and 11 for modified Grashof numbers of 2.31×10^4 and 1.78×10^5, respectively. The secondary flow velocity was defined as the flow velocity component in the x-y plane. It follows from Fig. 10 that the secondary flow patterns of the different aspect ratios were similar at a low modified Grashof number (2.31×10^4). Near the inlet of the channel, the hydrodynamic boundary layer was still developing, and the secondary flow was radial due to the viscous force. As the velocity of the fluid particles near the wall decreased, radial secondary flow was formed to satisfy mass conservation and the axial velocity at the core of the fluid increased consequently [41]. Buoyancy did not have a significant effect near the inlet, because the thermal boundary layer was thin and the temperature difference within the fluid was small. With the development of the hydrodynamic and thermal boundary layers along the channel length, the radial secondary flow became weaker and the vortical secondary flow caused by buoyancy effects became stronger. The secondary flow velocity gradually increased along the channel in the fully developed region due to the increased temperature and density differences.

The coloured arrows in Fig. 10 indicate that the highest secondary flow velocity was found in $AR = ½$. As the height of $AR = ½$ was the largest, the fluid particles could accelerate for a longer distance due to the buoyancy force, which increased the secondary flow velocity. The local secondary flow velocity was found to be higher near the lateral walls for $AR = 1$ and $AR = 2$ because of the high local temperature gradient, while the maximum local secondary flow velocity for $AR = ½$ was found at the centre. It can also be observed that the secondary flow velocity at the centre of the channel increased as the aspect ratio decreased. The reason for this is that as the width of the channel decreased, the distance between the two vortices became smaller, which in turn resulted in a stronger interaction with each other due to viscous effects and the acceleration of the fluid particles at the centre.

At the higher modified Grashof number of 1.78×10^5 in Fig. 11, the vortical flow has already formed in the upper half of the channel at $z/D = 11.75$, while radial flow still existed in the lower half. The flow patterns from $z/D = 61$ to $z/D = 623$ were similar to those at a lower modified Grashof number, although the secondary flow velocity was greater. At $z/D = 1248$, the flow patterns of the different aspect ratios exhibited different trends due to the formation of secondary vortex pairs. Strong upward flow of the secondary vortices was observed in $AR = 1$ and $AR = 2$ at $z/D = 1373$ where the secondary vortices became stable, with the highest local secondary flow velocity as indicated by the red arrows in Fig. 11. It is worth noting that the hot fluid only reached 40 % of the channel height in $AR = 1$ because of the strong downward flow of the primary vortices and temperature decrease. For $AR = 2$, the secondary flow velocity was lower, and the primary vortices were relatively far from each other, allowing more space for the formation of secondary vortices. Therefore, the secondary vortex pair were larger and

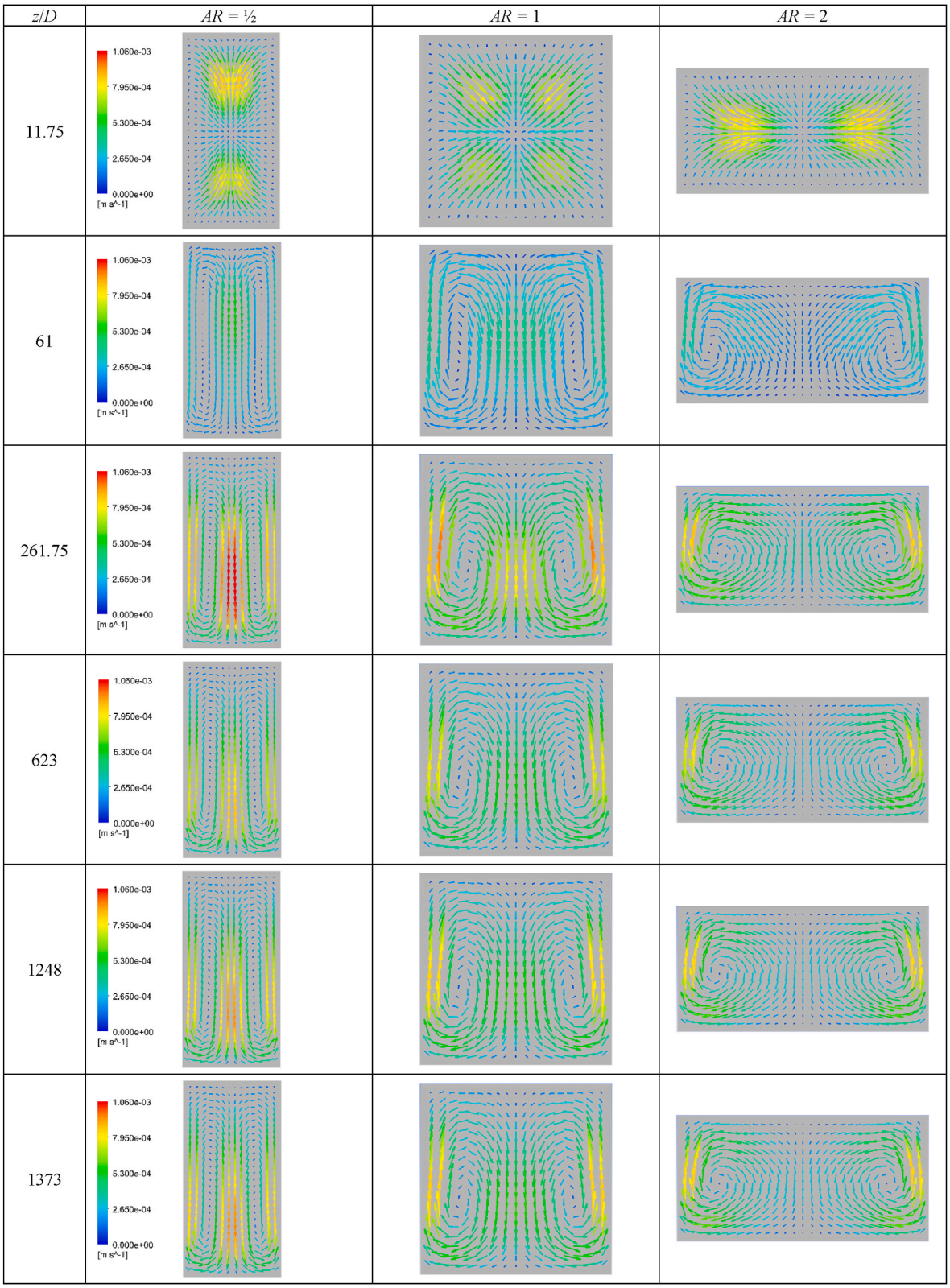

Fig. 10. Cross-sectional velocity profile [m/s] at different axial positions in the 8 mm channels at $Gr^* = 2.31 \times 10^4$ ($Re = 1800$, $\dot{q} = 1$ kW/m^2).

reached 55 % of the channel height. As the average fluid temperature increased further, the secondary vortex pair grew larger and became stronger due to combined effect of the increased density difference and interaction with the primary vortices.

The secondary vortex pair did not form at lower modified Grashof numbers (Fig. 10) as the temperature and density differences near the bottom of the channel were not sufficient. Similarly, only primary vortices existed for $AR = ½$. The large channel height and small width favoured the buoyancy effects, hence the strong primary vortices and good mixing within the fluid lowered the density difference and

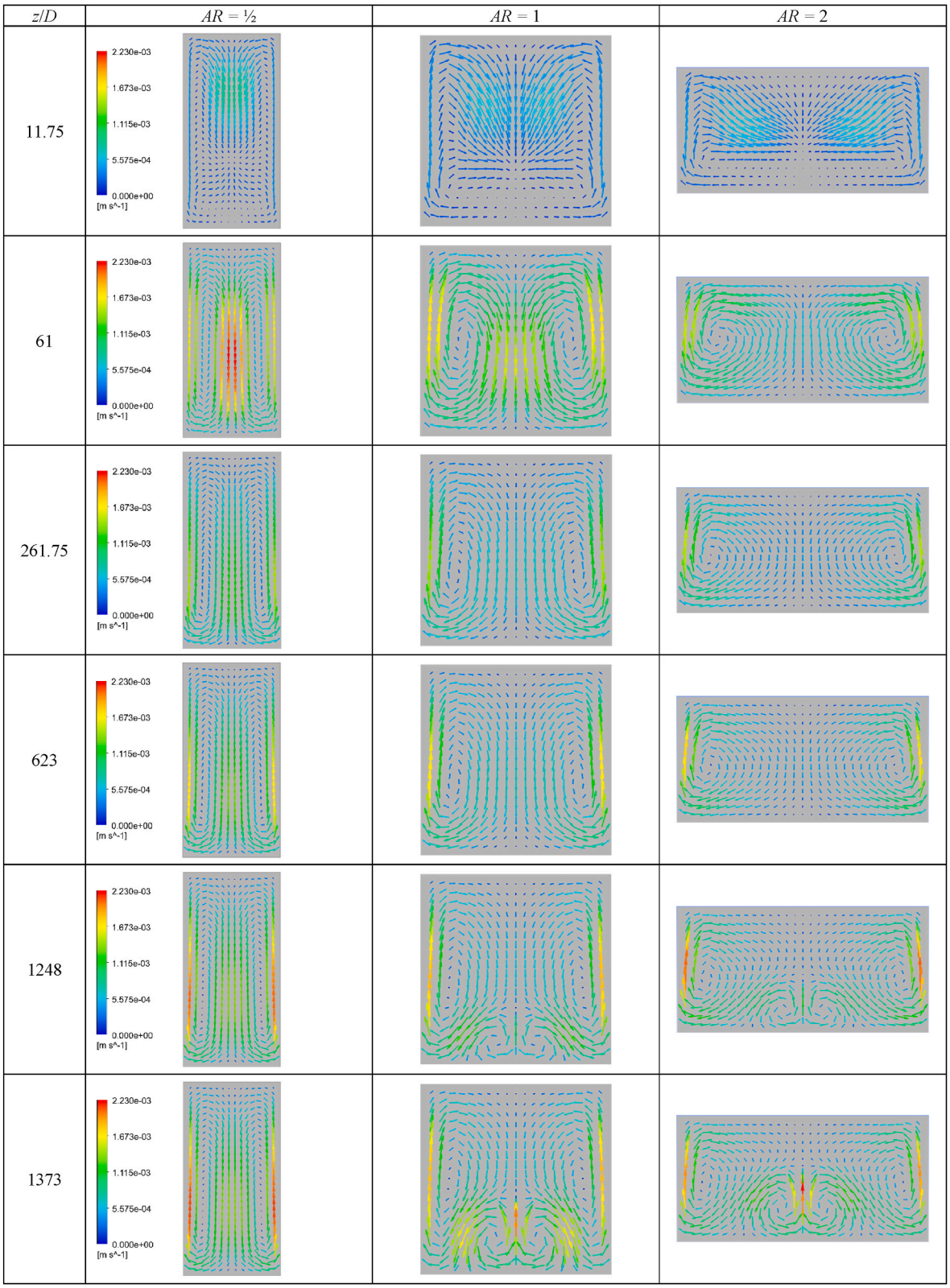

Fig. 11. Cross-sectional velocity profile [m/s] at different axial positions in the 8 mm channels at $Gr^* = 1.78 \times 10^5$ ($Re = 1000$, $\dot{q} = 3$ kW/m^2).

hindered the formation of secondary vortices. In addition, as the primary vortices were very close to each other and covered almost the entire cross-sectional area, there was little space for a secondary vortex pair to form. By contrast, in $AR = 1$ and $AR = 2$, the primary vortices were weaker and only covered about 90 % and 70 % of the cross-sectional area, respectively, leaving the top and bottom centre areas for the warmer fluid to accumulate. As indicated in Fig. 5(c), for increased hydraulic diameters and/or Grashof numbers in sufficiently long channels, a secondary vortex pair could also form in $AR = ½$.

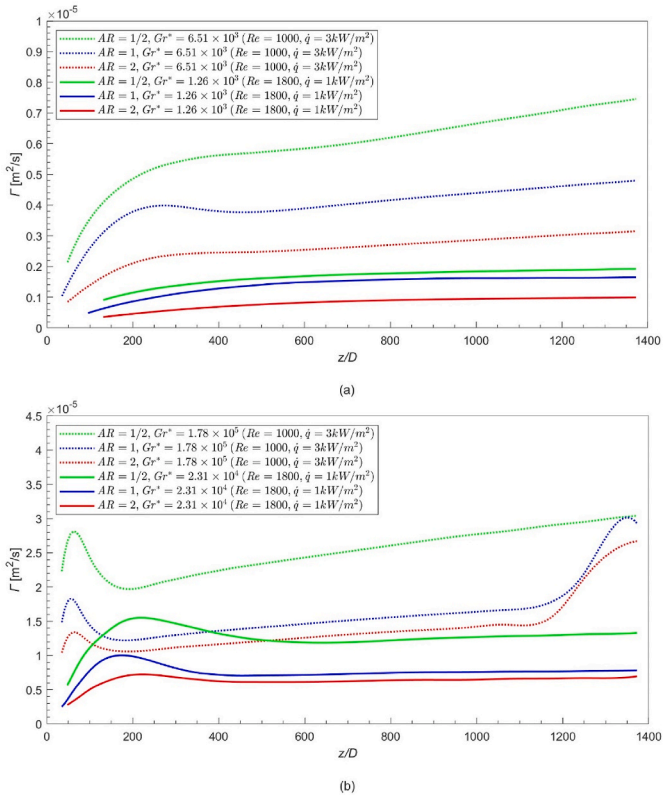

Fig. 12. Combined circulation strength at different axial positions in the (a) 4 mm and (b) 8 mm channels at different modified Grashof numbers.

4.2.3. Circulation strength

To quantitively investigate the development of the vortices along the channels, the circulation strength was calculated at different axial locations along the 4 mm and 8 mm channels and compared in Fig. 12(a) and (b), respectively. Due to the lower modified Grashof numbers in the 4 mm channels, there were only minor buoyancy effects at a modified Grashof number of 1.26×10^3, as evident by the relatively low circulation strengths. The circulation strength increased gradually along the channel and became constant at $z/D = 1000$. As expected from the local Nusselt number trends in Fig. 5(a), $AR = ½$ had the greatest circulation strength of 1.92×10^{-6} m^2/s, while $AR = 2$ had the lowest of 9.92×10^{-7} m^2/s. This was caused by the small channel height, large inactive area at the top, and weak interaction between the vortices, as discussed in Section 4.2.2. Since forced convection was predominant in this case, the circulation strength did not significantly affect the local Nusselt numbers.

At a higher modified Grashof number of 6.51×10^3, the trend remained similar while the magnitude of the circulation strength was greater because of the increased buoyancy effects. After the rapid increase near the inlet, the gradient of $AR = 1$ decreased between $z/D = 250$ and $z/D = 500$ and even became negative. The main reason for this was the reduction of the low temperature region in the centre of the channel. With the development of vortical flow, the warmer fluid was continuously transferred to the top of the channel, which caused the low temperature region to decrease and shift downwards, as indicated by Fig. 8. Therefore, the density difference decreased, particularly in the upper 2/3 of the channel, leading to weaker downward flow at the centre and a reduction in the circulation strength. For $z/D > 600$, the circulation strength gradually increased because of the increasing density gradient caused by the rapid temperature increase along the channel. The maximum circulation strength of 7.46×10^{-6} m^2/s in $AR = ½$ was almost 3 times higher than for the low modified Grashof number case. As the buoyancy effects became more significant, the circulation strength became the controlling factor of the local Nusselt number. Hence $AR = ½$ with the highest circulation strength had the highest Nusselt number.

In the 8 mm channels, the circulation strength was an order of magnitude higher than for the 4 mm channels, which was as expected from the modified Grashof numbers being an order of magnitude greater too. For $AR = ½$ and a modified Grashof number of 2.31×10^4, the circulation strength increased rapidly due to the increased buoyancy effects for $z/D < 200$. After reaching a peak, due to the significant cross-sectional mixing, the density difference within the fluid decreased, and the circulation strength decreased consequently. At $z/D = 600$, the secondary flow velocity and the density gradient reached a balance, hence the circulation strength no longer decreased but gradually increased along the channel length due to the increasing density gradient and temperature along the channel caused by the constant heat flux boundary condition. At $z/D = 1373$, the circulation strength of $AR = 1$ and $AR = 2$ were similar, 6.95×10^{-6} m^2/s and 7.81×10^{-6} m^2/s, respectively, while for $AR = ½$ it was 1.33×10^{-5} m^2/s. This indicates an increase of 91.4 % and 70.3 % compared to $AR = 1$ and $AR = 2$, which corresponds to the high secondary flow velocity in Fig. 7 and confirming the strongest secondary flow and the greatest buoyancy effects in $AR = ½$.

The gradient of the dotted lines for a modified Grashof number of 1.78×10^5 in Fig. 12(b) was significantly steeper than the solid lines for a modified Grashof number of 2.31×10^4 for all aspect ratios. Furthermore, in the entrance region, the circulation strength reached a peak earlier for increasing modified Grashof numbers. This agrees well with the findings of Everts and Meyer [28], namely that buoyancy effects assisted the development of the thermal boundary layer. After the decrease, it increased again along the channel due to the fast-increasing density gradient caused by the high heat flux. Once the secondary vortex pair formed at approximately $z/D = 1200$, the circulation strength increased significantly, and even doubled. For $AR = 1$, the circulation strength became within 3.8 % of that of $AR = ½$. However, as indicated by Fig. 5(b), the Nusselt number of $AR = 1$ exceeded that of $AR = ½$, because of the better overall cross-sectional mixing of the secondary vortices which compensated for the small difference of circulation strength. For $AR = 2$, the circulation strength was 12.2 % lower than for $AR = ½$, while the Nusselt number was 4.4 % lower. It can be concluded that more uniform cross-sectional mixing caused by the additional vortex pairs is more efficient than a single pair of strong vortices, when the total circulation strength was similar. This also explains why the local Nusselt numbers of the circular tube in Fig. 5(a) were higher than for the non-circular channels.

To gain a better understanding of the development and interaction of the primary and secondary vortices, Fig. 13 compares the magnitude of the circulation strength of the primary and secondary vortices in $AR = 1$

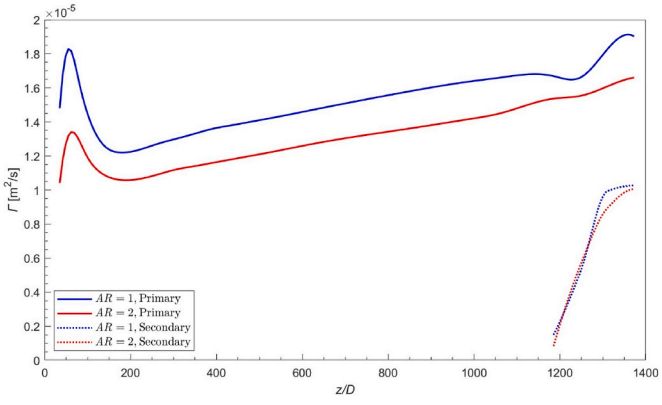

Fig. 13. Circulation strength of the primary and secondary vortices along the 8 mm channels at $Gr^* = 1.78 \times 10^5$ ($Re = 1000$, $\dot{q} = 3$ kW/m^2).

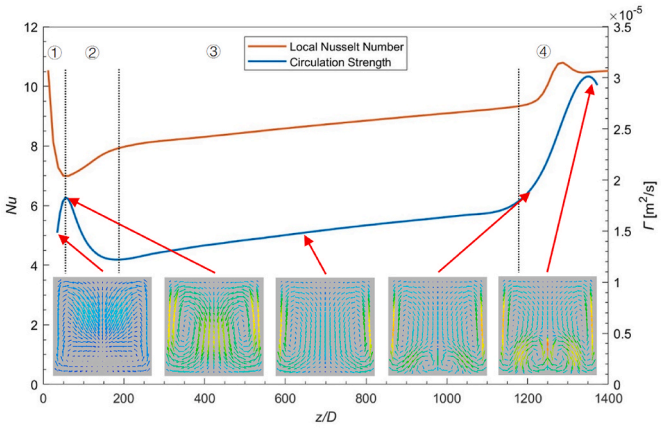

Fig. 14. Total circulation strength and local Nusselt number at different axial positions in the 8 mm channel with $AR = 1$ at $Gr^* = 1.78 \times 10^5$ ($Re = 1000$, $\dot{q} = 3$ kW/m^2).

and $AR = 2$ for the 8 mm channel and a Grashof number of 1.78×10^5. This figure indicates that the primary vortices in $AR = 1$ were stronger than for $AR = 2$ due to higher secondary flow velocity, as discussed in Section 4.2.2. Between $z/D = 1130$ and $z/D = 1230$, the circulation strength of the primary vortices in $AR = 1$ decreased slightly from 1.68×10^{-5} m^2/s to 1.65×10^{-5} m^2/s. A similar, but more subtle trend was also observed for $AR = 2$. For both channels, this was caused by the formation of the secondary vortex pair. As the secondary vortices formed, part of the downward flow in the centre of the channel moved towards the bottom centre area instead of towards the corners. Therefore, the peripheral flow of the primary vortices joined the secondary vortices, which resulted in the decrease in circulation strength of the primary vortices. Since the primary vortices in $AR = 2$ were further apart than for $AR = 1$, a smaller proportion of the peripheral flow from primary vortices joined the secondary vortices and hence the influence on the primary vortices was smaller.

At $z/D = 1230$, the secondary vortices had grown sufficiently to reach a balance, as indicated in Figs. 8 and 11, and the flow in the primary vortices no longer joined the secondary vortices. The circulation strength of both the primary and secondary vortices continued to increase due to increasing temperatures and density gradients. The secondary vortices approached an asymptotic value around $z/D = 1310$ and reached circulation strengths of 1.03×10^{-5} m^2/s and 1.01×10^{-5} m^2/s, respectively, for $AR = 1$ and $AR = 2$ at $z/D = 1373$. The circulation strength of the secondary vortices was almost identical because of the similar density difference at the centre bottom. The circulation strength of the primary vortices was 1.90×10^{-5} m^2/s and 1.66×10^{-5} m^2/s for $AR = 1$ and $AR = 2$, respectively. Therefore, the secondary vortices contributed to 37.8 % of the total circulation strength in $AR = 2$, while for $AR = 1$ it was 35.2 %, because of the stronger primary vortices.

Fig. 14 emphasises the significant effect of the circulation strength on the local Nusselt number trends for developing mixed convective flow, where the local Nusselt number and total circulation strength (including the primary and secondary vortex pairs) for $AR = 1$ in the 8 mm channel are compared at a modified Grashof number of 1.78×10^5. Furthermore, the cross-sectional profiles of the secondary flow vectors have also been included at specific axial positions to show the trends in the different regions. In region 1, as the radial secondary flow decreased and vortical secondary flow developed, the mixing effect was weak and the local Nusselt number decreased along the channel length. At $z/D = 48$, the circulation strength and local Nusselt number reached their peak and trough, respectively. Thereafter, in region 2, the wall-fluid temperature difference (as shown in Fig. 7) and circulation strength decreased due to the increased mixing inside the channel which also caused the local Nusselt numbers to increase. In region 3, where the secondary flow and density difference reached a balance, both the circulation strength and local Nusselt numbers increased gradually along the channel length as the temperature increased. In region 4, the secondary pair of vortices formed, which led to a significant increase in the total circulation strength and the local Nusselt numbers.

4.3. Influence of heat flux

After gaining a fundamental understanding the development of mixed convective flow in non-circular channels, Fig. 15 compares the local Nusselt number along the 8 mm channel at a Reynolds number of 1000, for heat fluxes ranging from 1 to 3 kW/m^2. The solid lines represent a heat flux of 1 kW/m^2, while the dashed-dot and dotted lines represent heat fluxes of 2 kW/m^2 and 3 kW/m^2, respectively.

This figure indicates that as the heat flux is increased, the difference between the different aspect ratios increased as well. The local Nusselt numbers increased with increasing heat flux due to the increased wall-fluid temperature differences and density differences which led to enhanced secondary flow and mixing. At heat fluxes of 1 and 2 kW/m^2, the magnitude of the local Nusselt numbers at a specific axial position increased as the aspect ratio was decreased from 2 to ½, which corresponded to the trends of the circulation strength in Fig. 12(b). However, at a heat flux of 3 kW/m^2, $AR = 1$ outperformed $AR = ½$ due to the formation of the secondary vortex pair.

4.4. Influence of Reynolds number

To investigate the effect of Reynolds number on the local Nusselt numbers of mixed convective laminar flow in non-circular channels,

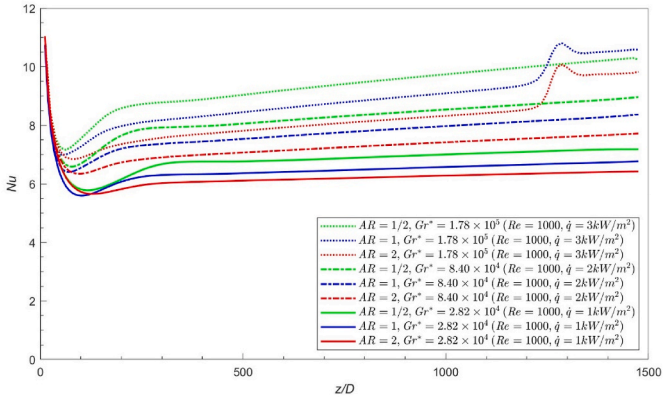

Fig. 15. Local Nusselt number at different axial positions in the 8 mm channels at different heat fluxes and a Reynolds number of 1000.

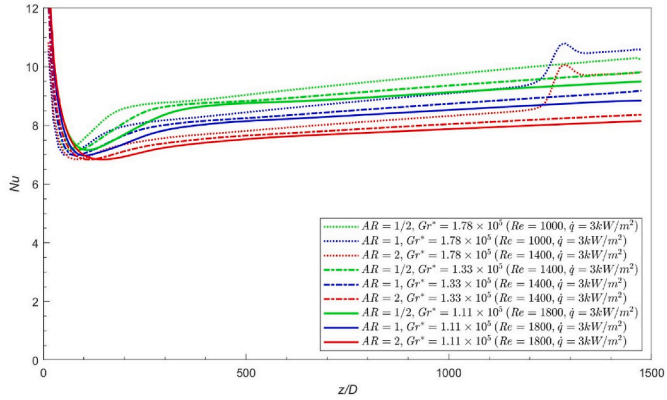

Fig. 16. Local Nusselt number along the 8 mm channel at different Reynolds numbers and a constant heat flux of 3 kW/m^2.

Fig. 16 compares the results for Reynolds numbers of 1000, 1400 and 1800 in the 8 mm channel heated at a constant heat flux of 3 kW/m^2. The dotted lines represent a Reynolds number of 1000, while the dashed-dot and solid lines represent Reynolds numbers of 1400 and 1800, respectively. As expected, this figure indicates that the enhancement of buoyancy effects became more significant for decreasing Reynolds numbers.

Near the inlet of the channels, the local Nusselt number increased with increasing Reynolds number. This was due to the flow being developing and the thermal entrance length increasing with Reynolds number. As the flow developed along the channel length and approached fully developed flow, an increase in Reynolds number led to a decrease in local Nusselt number. This was because the secondary flow was suppressed by the higher fluid velocities and smaller cross-sectional temperature and density differences. At a fixed Reynolds number, the local Nusselt numbers of $AR = ½$ were the highest, except at a Reynolds number of 1000 when they were exceeded by $AR = 1$ due to the formation of the secondary vortex pair. Overall, $AR = 2$ had the lowest local Nusselt numbers due to the lower secondary flow, as indicated by circulation strength in Fig. 12(b). For Reynolds number less than 1000, it is expected that the Nusselt number would further increase due to increased wall-fluid temperature differences and a secondary vortex pair to develop for $AR = ½$.

4.5. Multi-channel systems

After investigating the heat transfer characteristics through single channels, multiple channels were considered in a larger system. As this study focused specifically on a constant heat flux boundary condition, the approximately constant wall-fluid temperature difference could be translated to a counterflow heat exchanger where the temperature difference between the hot and the cold fluids have an approximately linear relationship to each other. Four different counterflow multi-channel systems where investigated, as illustrated in Fig. 17. The AR was varied between ½, 1 and 2 and heating was applied either from the sides or from the top and bottom surfaces, while the hydraulic diameter was fixed to 11.5 mm. The direction of heating in combination with the direction of the gravity influenced mixed convective flow. In Fig. 17(a), for $AR = 1$, a cold fluid stream only received heating from the top and bottom surfaces, while the channels in Fig. 17(b) were heated from the left and right sides. Fig. 17(c) represents a channel with $AR = 2$ which is heated from the top and bottom surfaces, while the channel with $AR = ½$ in Fig. 17(d) is heated from the left and right surfaces.

Fig. 18 compares the local Nusselt numbers of the four systems at a Reynolds number of 1800. For comparison purposes, the single channel results of the different aspect ratios were also included using solid lines. To ensure comparable conditions, the heat input to the respective channel in the multi-channel system, as well as the comparable single channel, was fixed to 1000 W. Therefore, to keep the heat input the same, the heat flux was increased for the multi-channel systems to compensate for the smaller heat surface area.

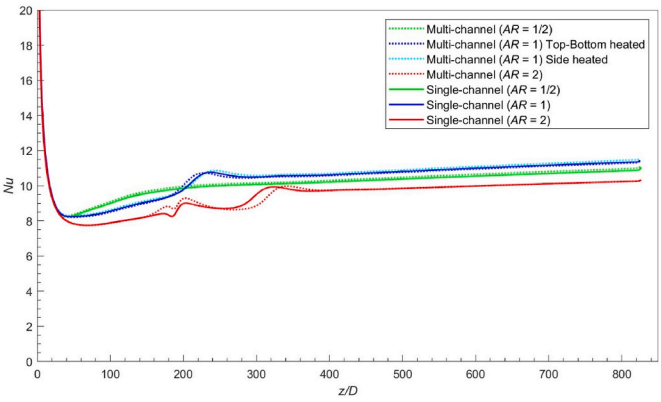

Fig. 18. Local Nusselt numbers as a function of axial position for a single channel (solid lines) and multi-channel (dotted lines) system for different aspect ratios at a Reynolds number of 1800 and heat input of 1000 W for $AR = ½$, 1, and 2.

A general trend in Fig. 18 is that for a fixed heat input and Reynolds number, the multi-channel results correlated very well with the single channel results although the heating configuration was slightly different. For $AR = 1$, the local Nusselt numbers for the uniform circumferential heating, top-bottom heating and left-right heating, all collapsed onto each other. This was due the significant mixed convection conditions that existed inside the channels. Similar to a single channel, the formation of a second vortex pair also occurred for the multi-channel systems at $AR = 1$ and $AR = 2$, which led to local increases in the local Nusselt numbers. For $AR = 2$, a slight delay of approximately $z/D = 20$ was observed for the secondary vortex pair. These findings indicate that scalability can be effectively used for mixed convective flow to achieve significant computational savings. A single channel can be used to predict the local heat transfer characteristics through a multi-channel counter flow system, as long as the total heat input and Reynolds number remain similar. This was a valuable finding that can reduce simulation complexity, costs and time during complex heat exchanger designs.

5. Conclusions

This study numerically investigated mixed convective laminar flow in non-circular channels with different aspect ratios. Channels with hydraulic diameters of 4 mm, 8 mm, and 11.5 mm and aspect ratios of ½, 1, and 2 were investigated for different modified Grashof numbers by varying the Reynolds number and heat flux. The local Nusselt number, cross-sectional velocity profile, and temperature profile were obtained and analysed. It was found that for forced convective flow in the 4 mm

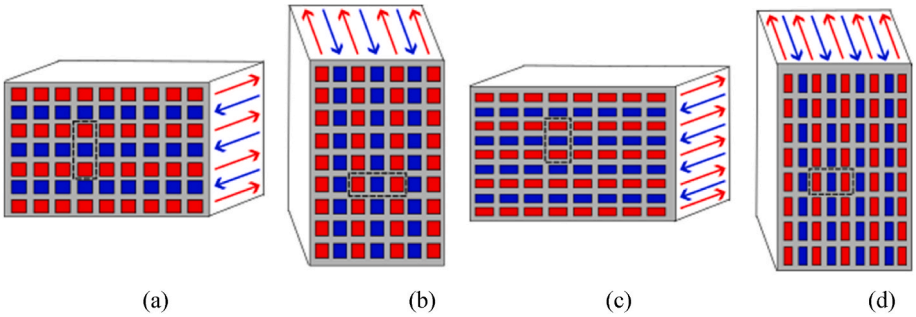

Fig. 17. Schematics of the counter flow multiple-channel systems with cold (blue) and hot (red) alternating layers. (a) $AR = 1$ heated from the top and bottom, (b) $AR = 1$ heated from the left and right sides, (c) $AR = 2$ heated from the top and bottom and (d) $AR = ½$ heated from the left and right sides. The respective sections that were investigated are marked with black dotted lines.

channels, the increased heat transfer surface area of $AR = ½$ and $AR = 2$ led to increased Nusselt numbers. When mixed convective flow existed at higher modified Grashof numbers, the vortices caused by buoyancy effects were stronger, and best heat transfer was achieved using $AR = ½$. The larger channel height favoured the buoyancy effects as the fluid particles could accelerate for a longer distance upwards. As the warmer fluid accumulated at the top of the channel, the colder fluid could not effectively remove heat from the top surface, leading to a lower secondary flow velocity and less mixing in the upper region. This explains why $AR = 1$ and $AR = 2$, with larger surface areas at the top, had lower Nusselt numbers. Hence $AR = ½$, with the smallest top surface and highest secondary flow velocity, had the highest local Nusselt numbers.

When the modified Grashof number was increased further by increasing the hydraulic diameter of the channels to 8 mm, a secondary vortex pair appeared near the bottom of $AR = 1$ and $AR = 2$. This was because of the large density difference caused by the accumulation of the warmer fluid and lower secondary flow velocity in that region. Consequently, $AR = 1$ had the highest Nusselt number of 10.5, which is a 191 % increase from that of forced convection, due to enhanced mixing caused by the secondary vortices. As the primary vortices were very strong and close to each other in $AR = ½$, a secondary vortex pair could not develop. Although only a single vortex pair existed in $AR = ½$, the Nusselt numbers remained greater than for $AR = 2$, indicating that an increase in vertical height is more favourable to enhance mixed convective flow than an increase in horizontal channel width. However, when hydraulic diameter was increased further to 11.5 mm, both the density difference and the horizontal channel width were sufficient for a secondary pair of vortices to form in $AR = ½$, which led to increased local Nusselt numbers.

To quantitively investigate the buoyancy-induced secondary flow, the circulation strength of the vortices was calculated along the channel. The circulation strength increased with increasing modified Grashof numbers, and increased rapidly near the channel inlets where the radial secondary flow vanished and vortical secondary flow was fast-developing due to high density gradient. After reaching a peak, the density gradient decreased due to the strong mixing effect by the vortical flow, leading to a reduction in circulation strength until a balance was reached. Thereafter it slowly increased due to the increasing density gradient caused by the temperature increase. The led to an increase in the local Nusselt numbers for mixed convective flow, unlike the decreasing Nusselt number trend for forced convective flow. The circulation strength increased with decreasing aspect ratio as well as with the formation of the secondary vortex pair. Due to the existence of the secondary vortex pair at $AR = 1$ in the 8 mm channel, the secondary flow strength of $AR = ½$ and $AR = 1$ were similar. However, the Nusselt number of $AR = ½$ was exceeded by $AR = 1$ due to the more uniform cross-sectional mixing caused by the secondary vortex pairs, indicating the importance of uniform cross-sectional mixing. Moreover, the channel width was found to be the key factor determining the formation of secondary vortices, and when the channel width and density gradient are both large enough, secondary vortices would form at the centre bottom.

Furthermore, the local Nusselt numbers increased with increasing heat flux because of the higher temperature and density gradients, while increasing the Reynolds number suppressed the buoyancy effects and led to decreased Nusselt numbers. The single channel results were also compared to a multi-channel counterflow heat exchanger system to investigate the scalability of the results. It was found that for a fixed heat input, the single- and multi-channel results correlated very well, indicating potential computational savings when designing larger heat exchanger systems.

Overall, it was concluded that mixed convective flow through non-circular channels can be enhanced by increasing the hydraulic diameter of the channel, increasing the heat flux or decreasing the Reynolds number and that best heat transfer performance can be expected for $AR = ½$. However, the formation of secondary vortex pairs, less mixing near the corners of the channels and significant effect of the height and width of the channel on buoyancy effects, highlighted the complexity of mixed convective flow through non-circular channels compared to circular tubes. It is therefore recommended future studies also focus on developing flow regime maps for non-circular channels and investigate the effect of surface roughness, inlet geometries, wider heat flux and Reynolds number ranges, as well as the transient behaviour of the vortex pairs and the transition to turbulence. This will provide valuable insights into optimising the heat transfer performance of compact heat exchangers containing non-circular channels. Furthermore, improving the empirical Nusselt number correlations for mixed convective flow will greatly benefit the design of heat exchangers as guided by industry standards.

CRediT authorship contribution statement

Qi Chen: Writing – original draft, Visualization, Validation, Software, Investigation, Formal analysis. **Nikha Harris:** Validation, Software, Investigation, Formal analysis. **Ken J. Craig:** Writing – review & editing, Supervision, Software, Resources, Methodology. **Marilize Everts:** Writing – review & editing, Supervision, Resources, Methodology, Funding acquisition, Conceptualization.

Declaration of competing interest

The authors declare that they have no known competing financial interests or personal relationships that could have appeared to influence the work reported in this paper.

Acknowledgement

This work was supported by the National Research Foundation (Grant Number: 116623), Department of Science and Innovation (DSI), the University of Pretoria and the University College London. The authors would additionally like to acknowledge the Centre for High Performance Computing (CHPC) in Cape Town, South Africa, as well as the University College London, which made these simulations achievable.

Data availability

Data will be made available on request.

References

[1] A. Moradikazerouni, M. Afrand, J. Alsarraf, O. Mahian, S. Wongwises, M.-D. Tran, Comparison of the effect of five different entrance channel shapes of a microchannel heat sink in forced convection with application to cooling a supercomputer circuit board, Applied Thermal Engineering, 1078–1089, https://doi.org/10.1016/j.applthermaleng.2019.01.051, 2019.

[2] M.E. Arzutuğ, Design of a CPU heat sink with minichannel-fins & its thermal analysis, polish journal of chemical technology. https://doi.org/10.2478/pjct-2023-0029, 2023.

[3] A.P.C. Sarmiento, V.H.T. Soares, G.G. Carqueja, J.V.C. Batista, F.H. Milanese, M.B. H. Mantelli, Thermal performance of diffusion-bonded compact heat exchangers, International Journal of Thermal Sciences, 106384, https://doi.org/10.1016/j.ijthermalsci.2020.106384, 2020.

[4] Z. Deng, S. Zhang, K. Ma, C. Jia, Y. Sun, X. Chen, Y. Luo, B. Li, T. Li, Numerical and experimental study on cooling high power chips of data centers using double-side cooling module based on mini-channel heat sink, Applied Thermal Engineering, 120282, https://doi.org/10.1016/j.applthermaleng.2023.120282, 2023.

[5] W. Li, X. Peng, M. Xiao, A. Garg, L. Gao, Multi-objective design optimization for mini-channel cooling battery thermal management system in an electric vehicle, International Journal of Energy Research. https://doi.org/10.1002/er.4518, 2019.

[6] A. Babaei, E. Aminian, H. Saffari, Enhanced heat transfer performance in a parabolic trough solar collector: a CFD investigation of silver and copper nanofluids utilizing porous medium, Proceedings of the Institution of Mechanical Engineers, Part E: journal of Process Mechanical Engineering. https://doi.org/10.1177/09544089241289072, 2024.

[7] I.A. Stogiannis, A.A. Mouza, S.V. Paras, Efficacy of SiO2 nanofluids in a miniature plate heat exchanger with undulated surface, International Journal of Thermal Sciences, 230–238, https://doi.org/10.1016/j.ijthermalsci.2015.01.035, 2015.

[8] S.K. Mylavarapu, X. Sun, R.N. Christensen, R.R. Unocic, R.E. Glosup, M. W. Patterson, Fabrication and design aspects of high-temperature compact diffusion bonded heat exchangers, Nuclear Engineering and Design, 49–56, https://doi.org/10.1016/j.nucengdes.2011.08.043, 2012.
[9] A. Bertinetti, K.A. Avramidis, F. Albajar, F. Cau, F. Cismondi, Y. Rozier, L. Savoldi, R. Zanino, Multi-physics analysis of a 1MW gyrotron cavity cooled by mini-channels, Fusion Engineering and Design, 313–316, https://doi.org/10.1016/j.fusengdes.2017.05.016, 2017.
[10] D.B. Tuckerman, R.F.W. Pease, High-performance Heat Sinking for VLSI, IEEE, Electron Device Letters, 1981, pp. 126–129, https://doi.org/10.1109/EDL.1981.25367.
[11] M.U. Sajid, H.M. Ali, A. Sufyan, D. Rashid, S.U. Zahid, W.U. Rehman, Experimental investigation of TiO2–water nanofluid flow and heat transfer inside wavy mini-channel heat sinks, J. Therm. Anal. Calorim. (2019) 1279–1294, https://doi.org/10.1007/s10973-019-08043-9.
[12] D.R. Oliver, The effect of natural convection on viscous-flow heat transfer in horizontal tubes, Chem. Eng. Sci. (1962) 80035–80039, https://doi.org/10.1016/0009-2509(62.
[13] B. Parizad Benam, A.K. Sadaghiani, V. Yağcı, M. Parlak, K. Sefiane, A. Koşar, Review on high heat flux flow boiling of refrigerants and water for electronics cooling, Int. J. Heat Mass Tran. (2021) 121787, https://doi.org/10.1016/j.ijheatmasstransfer.2021.121787.
[14] P. Vasileiadou, K. Sefiane, T.G. Karayiannis, J.R.E. Christy, Flow boiling of ethanol/water binary mixture in a square mini-channel, Appl. Therm. Eng. (2017) 1617–1626, https://doi.org/10.1016/j.applthermaleng.2017.08.126.
[15] M. Venter, A. Widyatama, J. Dirker, K. Sefiane, Flow boiling in a rectangular micro/mini channel with self-rewetting and non-rewetting fluids, Int. J. Heat Mass Tran. (2024) 126189, https://doi.org/10.1016/j.ijheatmasstransfer.2024.126189.
[16] A. Babaei, E. Aminian, H. Saffari, Numerical study of heat transfer and pressure drop of nanofluids in a combined porous media of hydrophobic and hydrophilic surfaces, Proceedings of the Institution of Mechanical Engineers, Part A, Journal of Power and Energy (2023) 1308–1328, https://doi.org/10.1177/09576509231158668.
[17] H.R. Talesh Bahrami, E. Aminian, H. Saffari, Energy transfer enhancement inside an annulus using gradient porous ribs and nanofluids, journal of energy Resources technology. https://doi.org/10.1115/1.4047312, 2020.
[18] M. Siavashi, H.R. Talesh Bahrami, E. Aminian, Optimization of heat transfer enhancement and pumping power of a heat exchanger tube using nanofluid with gradient and multi-layered porous foams, Appl. Therm. Eng. (2018) 465–474, https://doi.org/10.1016/j.applthermaleng.2018.04.066.
[19] E. Aminian, H. Moghadasi, H. Saffari, A.M. Gheitaghy, Investigation of forced convection enhancement and entropy generation of nanofluid flow through a corrugated minichannel filled with a porous media, Entropy (2020) 1008, https://doi.org/10.3390/e22091008.
[20] M. Sedighi, A. Ayoobi, E. Aminian, Numerical investigation on forced convection enhancement within an oil cooler through the simultaneous use of porous media and nanofluid, Proceedings of the Institution of Mechanical Engineers, Part E: Journal of Process Mechanical Engineering (2024) 331–341, https://doi.org/10.1177/09544089221143895.
[21] M.A. Khalifa, H.M. Jaffal, Influence of pin fins and channel geometry on the hydrothermal performance of hexagonal mini-channel heat sink for cooling cylindrical batteries, Case Stud. Therm. Eng. (2024) 105336, https://doi.org/10.1016/j.csite.2024.105336.
[22] A. Torbatinezhad, Y. Pahamli, M.J. Hosseini, R. Bahrampoury, Influence of the zigzag fins and inlet arrangements on the cooling proficiency of the mini-channel heat sink, Propulsion and Power Research (2024) 194–206, https://doi.org/10.1016/j.jppr.2024.05.002.
[23] P. Qi, D. Jing, Experimental and numerical study on the hydrothermal performances of a mirror Y-shaped convergent mini-channel heat sink, Case Stud. Therm. Eng. 53 (2024) 103966, https://doi.org/10.1016/j.csite.2023.103966.
[24] H.A. Hussein, Numerical hydrothermal evaluation of heat transfer in a multi-mini-channel heat sink: effect of square pin fins, Results in Engineering (2023) 101403, https://doi.org/10.1016/j.rineng.2023.101403.
[25] T.G.K. Alişan Gönül, Pressure Drop, Heat Transfer, Characteristics in a microchannel with pin-fins, J. Fluid Flow Heat Mass Tran. (2024) 187–196, https://doi.org/10.11159/jffhmt.2024.019.
[26] Amirah Mohamad Sahar M, S.A.I., jan wissink, mohamed M. Mahmoud, tassos G. Karayiannis, flow distribution in parallel rectangular multi microchannels in single phase, CFD Lett. (2023) 67–75, https://doi.org/10.37934/cfdl.15.1.6775.
[27] J.P. Meyer, M. Everts, Single-phase mixed convection of developing and fully developed flow in smooth horizontal circular tubes in the laminar and transitional flow regimes, Int. J. Heat Mass Tran. (2018) 1251–1273, https://doi.org/10.1016/j.ijheatmasstransfer.2017.10.070.
[28] M. Everts, J.P. Meyer, Laminar hydrodynamic and thermal entrance lengths for simultaneously hydrodynamically and thermally developing forced and mixed convective flows in horizontal tubes, Exp. Therm. Fluid Sci. (2020), https://doi.org/10.1016/j.expthermflusci.2020.110153.
[29] M. Everts, J.P. Meyer, Relationship between pressure drop and heat transfer of developing and fully developed flow in smooth horizontal circular tubes in the laminar, transitional, quasi-turbulent and turbulent flow regimes, Int. J. Heat Mass Tran. (2018) 1231–1250, https://doi.org/10.1016/j.ijheatmasstransfer.2017.10.072.
[30] J.D. Jackson, M.A. Cotton, B.P. Axcell, Studies of mixed convection in vertical tubes, Int. J. Heat Fluid Flow (1989) 2–15, https://doi.org/10.1016/0142-727X(89)90049-0.
[31] J. Orfi, N. Galanis, C.T. Nguyen, Laminar fully developed incompressible flow with mixed convection in inclined tubes, Int. J. Numer. Methods Heat Fluid Flow (1993) 341–355, https://doi.org/10.1108/eb017535.
[32] R. Taher, M.M. Ahmed, Z. Haddad, C. Abid, Poiseuille-Rayleigh-Bénard mixed convection flow in a channel, Heat transfer and fluid flow patterns, International Journal of Heat and Mass Transfer (2021) 121745, https://doi.org/10.1016/j.ijheatmasstransfer.2021.121745.
[33] C. Dao, Numerical simulations of 3D-flow for laminar mixed convection in horizontal rectangular tubes, J. Eng. Thermophys. (2009) 141–143, https://doi.org/10.3321/j.issn:0253-231X.2009.01.039.
[34] A. Benallou, Forced convection inside non-cylindrical pipes, in: Energy Transfers by Convection (2018) 43–67, https://doi.org/10.1002/9781119476962.ch3.
[35] F. Koffi, C. Abid, F. Papini, Mixed convection flow in a horizontal rectangular channel subjected to a horizontal thermal gradient, Heat Mass Tran. (2011) 1251–1260, https://doi.org/10.1007/s00231-011-0775-y.
[36] K. Toriyama, K. Ichimiya, M. Kaneko, Effects of aspect ratio on mixed convection in a horizontal rectangular duct with heated and cooled side walls, Heat Tran. Asian Res. (2013) 544–555, https://doi.org/10.1002/htj.20391.
[37] C.O. Popiel, J. Wojtkowiak, Simple formulas for thermophysical properties of liquid water for heat transfer calculations (from 0°C to 150°C), Heat Tran. Eng. (1998) 87–101, https://doi.org/10.1080/01457639808939929.
[38] M. Everts, J.P. Meyer, Heat transfer of developing and fully developed flow in smooth horizontal tubes in the transitional flow regime, Int. J. Heat Mass Tran. (2018) 1331–1351, https://doi.org/10.1016/j.ijheatmasstransfer.2017.10.071.
[39] A. Benallou, Forced convection inside cylindrical pipes, in: Energy Transfers by Convection (2018) 15–41, https://doi.org/10.1002/9781119476962.ch2.
[40] Ansys®Fluent, Ansys Fluent Theory Guide, 2023. USA.
[41] M. Everts, M. Mahdavi, M. Sharifpur, J.P. Meyer, Simultaneous development of the hydrodynamic and thermal boundary layers of mixed convective laminar flow through a horizontal tube with a constant heat flux, Int. J. Therm. Sci. (2023) 108178, https://doi.org/10.1016/j.ijthermalsci.2023.108178.